Design and Simulation of Beam-Background Monitors in the Vicinity of the Electromagnetic Calorimeter for the Belle II Experiment

Andrea Fodor

Department of Physics

McGill University

Montreal, Quebec

March 2017

A thesis submitted to McGill University in partial fulfillment of the requirements of the degree of Master of Science

ACKNOWLEDGEMENTS

I would like to thank the Belle II collaboration for their dedication and expertise in running the Belle II project; my supervisor, Dr. Andreas Warburton, for giving me the opportunity to work on this exciting project, and for his continuous guidance and expertise he provided during the course of my studies; Dr. Steven Robertson for his advice and invaluable insights and guidance throughout my research; the Belle II group at Université de Montréal, Jean-Pierre Martin, Nikolai Starinski and Paul Taras, whose experience in detector design helped the selection of suitable detection techniques for this project, and whose testing of LYSO crystals provided a deeper insight into its intrinsic radioactivity; my colleague students at McGill, Waleed Ahmed, with whom I worked together on implementation of the background monitors in the Belle II simulation, Helena Pikhartova, for numerous discussions and help, and Robert Seddon, whose experience in analysis techniques provided great help. I would like to thank Alex Beaulieu at the University of Victoria for his help with the implementation of the simulation and his insightful advice. Lastly, I thank my family for their continuing unconditional support.

ABSTRACT

The upgrade of the KEKB to the SuperKEKB accelerator is being followed by the update of the Belle detector to the Belle II detector. The design instantaneous luminosity of SuperKEKB is $8{\cdot}10^{35}$ $\mathrm{cm}^{-2}\mathrm{s}^{-1}$, forty times higher than that at KEKB. The new high-luminosity environment will bring an increase in the beam background. Due to the 40-fold increase in luminosity, the beam backgrounds are expected to increase also by forty times compared to those encountered by the Belle experiment. The Belle II collaboration has implemented various countermeasures to combat the increase in beam background and enable a safe operation of the Belle II detector. A beam background monitoring system was needed for measuring the background levels in the vicinity of the electromagnetic calorimeter endcaps. The system will need to be sensitive to both the fast changing injection background and the more slowly changing DC-like background during regular collider operation. The focus of this thesis is the motivation of the design and technologies used for the background monitoring system. The existing background simulation for the calorimeter was analyzed in preparation for the beam background monitors' design. The monitors are to be placed in recesses located in the forward and backward endcap shields. LYSO scintillating crystals read out by Hamamatsu R7761-70 photomultipliers will be used for detection. The background monitors were included in the background simulation, which was used to estimate the energy deposition they will be receiving.

ABRÉGÉ

La mise à niveau du KEKB vers l'accélérateur SuperKEKB est suivit par celle du détecteur Belle vers Belle II. La luminosité instantanée du SuperKEKB est de $8{\cdot}10^{35}$ $\mathrm{cm}^{-2}\mathrm{s}^{-1}$, quarante fois plus élevée que celle du KEKB. Cette hausse en luminosité va s'accompagner d'une hausse de proportion semblable du bruit dans le faisceau par rapport à ce que l'expérience Belle observe actuellement . La Collaboration Belle II a déjà mis en place des contre-mesures pour assurer une opération sécuritaire du détecteur Belle II, ainsi qu'un environment optimale au niveau du bruit lumineux. Un système de monitorage est nécessaire pour mesurer le niveau de bruit proche des extrémités du calorimètre électromagnétique. D'une part, ce système doit être sensible au bruit transitoire dû à l'injection de particules dans le faisceau et d'autre part, au changement plus lent du bruit de fond DC. Cette thèse se concentre sur les designs et technologies pouvant être utilisés pour ce système de monitorage. La simulation existante du bruit dans le calorimètre est analysée en préparation à la conception du design des modules de monitorage. Ces derniers sont destinés à occuper des emplacements situés aux extrémités du détecteur. Des cristaux LYSO lues par des photomultiplicateurs Hamamatsu R7761-70 sont utilisés pour la détection. Les modules de monitorage du bruit sont inclus dans la simulation utilisée pour estimer la déposition en énergie qu'ils observeront en état d'opération.

Statement of Contribution

The presented work is my own, with the following exceptions: the background simulation for the Belle II detector was done by the Belle II collaboration; the raw data for the background simulation of the electromagnetic calorimeter was generated by Samuel de Jong; and the implementation of the background monitors in the GEANT4 simulation was done together with Waleed Ahmed.

TABLE OF CONTENTS

LIST OF TABLES

LIST OF FIGURES

CHAPTER 1
Introduction

The Belle II experiment at the SuperKEKB accelerator is scheduled to start data taking by the end of 2018. The upgrade of the KEKB accelerator to the SuperKEKB accelerator has the goal to increase the luminosity by 40 times. With this luminosity increase comes an increase in beam background. To adapt to the new high-luminosity environment of SuperKEKB, the Belle detector was upgraded to the Belle II detector. The goal of the Belle II experiment is to search for evidence of new physics beyond the Standard Model. It will perform high-precision measurements that include rare and forbidden decays in the Standard Model, and charge-parity violation in heavy quarks and leptons.

This thesis focuses on the design and simulation of a beam-background monitoring system that will be implemented in the vicinity of the endcaps of the electromagnetic calorimeter (ECL). Chapter 2 describes the design of SuperKEKB and its operation, together with the phased commissioning process that is implemented to investigate the new background environment in the upgraded collider. Chapter 3 explains the intention of the Belle II experiment and describes the design of each Belle II subdetector. Chapter 4 explains the mechanisms behind the most important background sources at the Belle II experiment, and the countermeasures implemented to reduce their effects. The initial design and the requirements for the beam-background monitoring system are explained in Chapter 5. Chapter 6 describes the analysis of the ECL

background simulation performed to better understand the environment in which the beam background monitors will operate. Based on the results of this simulation, the final design of the background monitors is described in Chapter 7, together with their implementation in the Belle II background simulation. The conclusion and future work are discussed in Chapter 8.

CHAPTER 2
The SuperKEKB accelerator

2.1 SuperKEKB overview

The SuperKEKB accelerator, located at the KEK High Energy Accelerator Research Organization in Tsukuba, Japan, is the upgrade of the existing KEKB accelerator. It collides electrons and positrons to produce B mesons, whose decays are then analyzed; it is thus called a B-factory. The KEKB accelerator was operational from 1999 to 2010. It accumulated more data than any other B-factory before, with integrated luminosity of 1000 fb^{-1} [1].

Electrons and positrons are accelerated such that the center of mass energy is equal to the mass of the $\Upsilon(4S)$ resonance. The $\Upsilon(4S)$ meson decays almost exclusively to $B\bar{B}$ pairs. The Low Energy Ring (LER) and the High Energy Ring (HER) contain the positron and electron beams, respectively. At the KEKB accelerator, the energies were 3.5 GeV for positrons and 8.0 GeV for electrons. At SuperKEKB, this asymmetry is somewhat smaller, with positron energy at 4.0 GeV and electron at 7.0 GeV. The center of mass energy is as follows:

$$E_{CM} = 2\sqrt{E_{LER}E_{HER}} = 10.58 \text{ GeV} = m_{\Upsilon(4S)}$$

The beam energy asymmetry is important to obtain a boosted frame for the outgoing particles. Since the outgoing pairs of B mesons have a total mass that is approximately equal to the mass of the resonance, they are produced at rest in the center of mass frame. To make their detection easier, an energy asymmetry is introduced, so that a boost is created in the center of mass frame. The induced Lorentz boost is

$$\beta\gamma = \frac{E_{HER} - E_{LER}}{E_{CM}} = 0.28$$

The schematic layout of the SuperKEKB collider is shown in Fig. 2–1. The electron beams are produced by irradiating a cold cathode with laser photons. They are then accelerated to 7.0 GeV in the linac and injected into the HER. The positrons are produced as secondary particles by shooting electrons at a tungsten target and are then injected to a damping ring where they are focused. After that, they are re-injected in the linac and accelerated to 4.0 GeV and injected into the LER.

SuperKEKB uses a "continuous injection" scheme. Electron and positron beams are injected in groups called bunches. After the initial injection of 2500 bunches spaced at 4 ns, the existing bunches are topped up by injecting charge to keep the bunch current close to constant. The continuous injection is necessary since the beam lifetime is short, on the order of 600 s [2]. Two topped-up bunches are separated by 100 ns, injected at 25 Hz. The beam bunches have a 10 µs revolution time around the 3016 m accelerator circumference. The topped up bunches produce high background levels during the first few turns in the accelerator. The Belle II detector is to remain in operation during injection, with the data acquisition system blocked for a short amount of time for the injected bunch only [1].

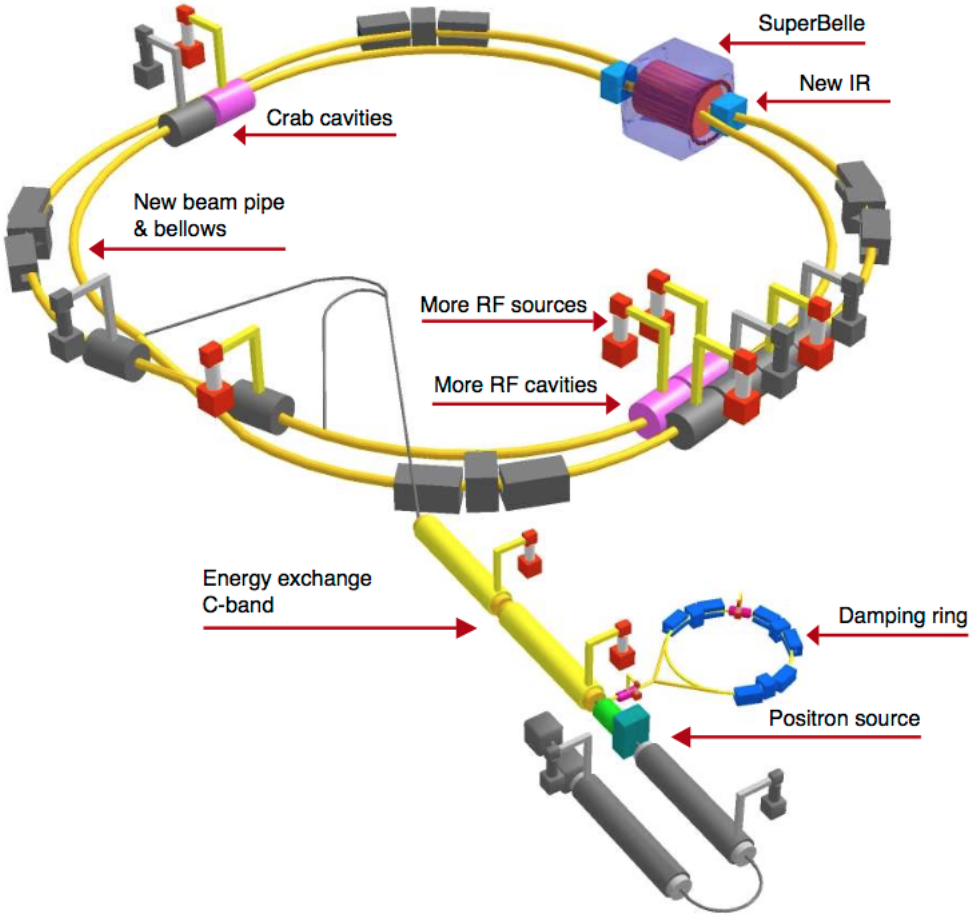

Figure 2–1: Schematic layout of the SuperKEKB [3].

2.2 Nano-beam scheme

The design luminosity of the SuperKEKB facility is 40 times higher than that of the previous KEKB version. It is designed to have a luminosity of $8{\cdot}10^{35}$ cm^{-2}s^{-1} [1]. In order to achieve this high luminosity, the "nano-beam" scheme was applied [2]. Each particle in the beam can be approximated as a harmonic oscillator with periodic restoring force, where the envelope of the motion is modulated by the amplitude, or beta, function [4]. The idea behind the nano-beam scheme is to squeeze the vertical beta function, β_y, at the Interaction Point (IP) by minimizing the longitudinal size of the overlap region of the two beams. The size of the overlap region, d, is considered to be the effective bunch length in the nano-beam scheme. As illustrated in Fig. 2–2, it is determined by the horizontal half crossing angle, ϕ, and the horizontal beam size at the IP, σ_x^*,

$$d \cong \frac{\sigma_x^*}{\phi}.$$

To shorten the length d, the Interaction Region (IR) was modified to a larger horizontal crossing angle of 83 mrad [1], and the horizontal beam size was increased by lowering the emittance. For a beam with a Gaussian distribution, the emittance is equal to the area in the position and momentum phase space containing one standard deviation σ_x of the beam's particles [4]. The large crossing angle also enables a quick separation of the two beams and allows the final quadrupole focusing magnets to be placed closer to the IP, which helps to achieve small beta function at the IP.

The accelerator luminosity is calculated as [1]

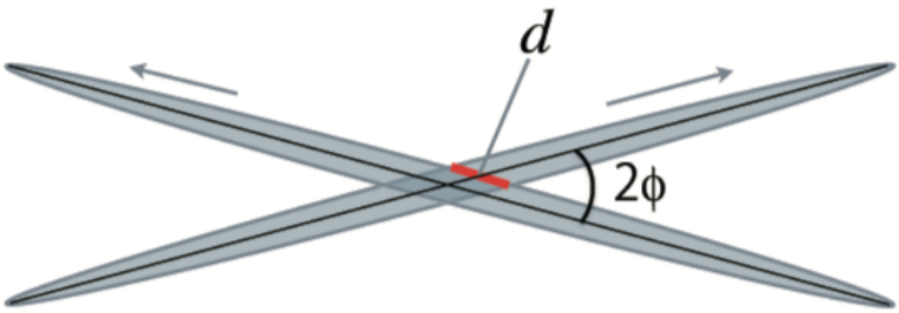

Figure 2–2: Schematic view of the beam intersection in the nano-beam scheme [1].

$$L = \frac{\gamma_\pm}{2er_e}\left(\frac{I_\pm \xi_{y\pm}}{\beta^*_{y\pm}}\right)\left(\frac{R_L}{R_{\xi_y}}\right),$$

where r_e and e are the electron classical radius and the elementary electric charge, $\gamma_\pm$ is the Lorentz factor and $\xi_{y\pm}$ the vertical beam-beam parameter, and $I_\pm$ the total beam current, + indicating the positron values and − the electron values. The $\xi_{y\pm}$ is the vertical beam-beam parameter and $\beta^*_{y\pm}$ is the vertical beta function at the interaction point. R_L and R_{ξ_y} are the reduction factors for the luminosity and the vertical beam-beam parameter, which arise from the non-zero crossing angle. Their ratio is close to unity. The beam-beam parameter ξ_y[1] is assumed to be the same as for KEKB. The β^*_y is smaller by a factor of 20. Thus, to obtain a 40 times higher luminosity, the total beam currents need to be double compared to those at KEKB. The increased beam current and the small beta function lead to a shorter beam

[1] The beam-beam parameter characterizes the strength of forces acting between the two beams; it is defined as a function of the ratio of current and the beam size at the collision point [5].

lifetime due to the Touschek effect, which is explained in more detail in Chapter 4. Since the Touschek effect is proportional to E^{-3} [1], the asymmetry in the beam energies was reduced.

2.3 The Commissioning Process

Because of the changes introduced, the SuperKEKB environment is not comparable to the KEKB. The predicted increase in background rate is 40 times [1]. The nano-beam scheme has never been used before, so there is no indication if these predictions are accurate. Changes are introduced to the design of the detectors close to the IP due to this increase in background. To make sure the beam behaviour is as expected and the electronics used are not damaged due to the high background rate, detailed simulation of the new environment is performed, and two commissioning stages, prior to the full Belle II experiment's operation, are introduced to further explore the beam behaviour.

2.3.1 Phase 1

The phase 1 of the commissioning process, performed from February till June 2016, includes the BEAST II (Beam Exorcism for A STable experiment II) detector [6]. It operated without the final focus quadrupole magnets (QCS) and without the Belle II detector. There were no beam collisions in this phase. The main goals in this period are to complete the basic machine commissioning including the commissioning of each accelerator component and to perform sufficient vacuum scrubbing before the Belle II detector is rolled in. During phase 1, the measurements of the injection backgrounds are also performed. This is especially important, as the injection

background was not included in the background simulation. Also, the background rates during regular operation are measured, together with the time profiles of the backgrounds for both HER and LER rings.

The schematic of the BEAST II detector is illustrated in Fig. 2–3. It contains

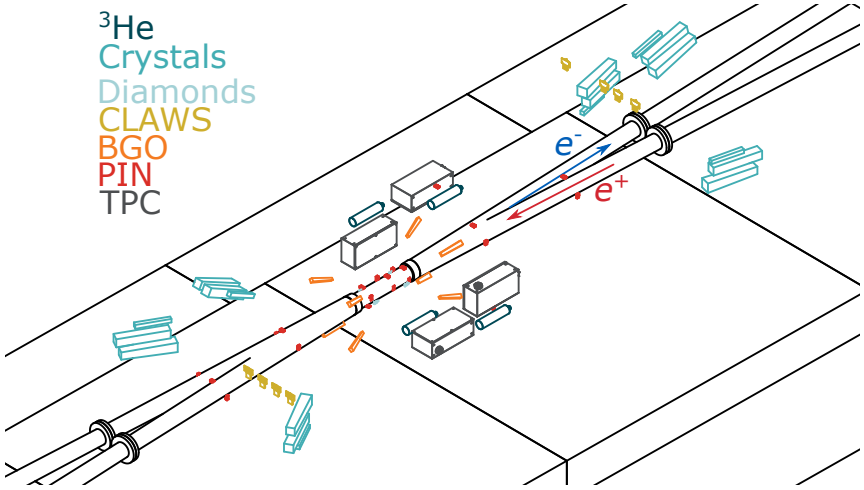

Figure 2–3: BEAST II detector schematic with sub-detectors indicated [7].

seven sub-detectors. An array of silicon PIN diodes, mounted on the beam-pipe, is used to monitor the ionizing radiation. The CLAWS detector consists of 8 plastic scintillator tiles read out with silicon photomultipliers. Its goal is to measure background levels connected to the injection with time resolution higher than the bunch crossing frequency. The Helium 3 system consists of four detectors, each a stainless steel cylinder filled with a ^{3}He gas mixture, with a sense wire at high voltage going through the center of the tube. The purpose of this sub-detector is the detection of

thermal neutrons[2] . The time projection chamber (TPC) is used to monitor the fast neutron flux component originating from the beam line. Its active volume is filled with a mixture of He and CO_2 gas. Mounted around the future interaction region are the BGO (Bismuth Germanate) crystals, which are used for luminosity monitoring. To validate the electromagnetic radiation simulation in the position of the endcaps of the electromagnetic calorimeter, six sets of scintillating crystals, each containing a caesium iodide (CsI), thallium doped caesium iodide (CsI(Tl)) and cerium doped lutetium-yttrium oxyorthosilicate (LYSO) crystal, is installed at the positions corresponding to the endcap crystals. Chemical Vapour Deposition (CVD) diamond sensors are installed on the beam-pipe and are used as fast luminosity monitors for feedback in presence of dynamical imperfections, so the beam running can be aborted.

2.3.2 Phase 2

The phase 2 will be performed with the Belle II detector rolled in and the QCS magnets in place. The Belle II vertexing detectors will not be installed, but the SuperKEKB machine parameters will be the same as in the final stage. It is needed to validate that the radiation level is safe before the vertexing detector's installation.The He3, TPC, PIN diodes and diamond sensors from phase 1 will continue operating in phase 2. An addition will be the PLUME detector, a double sided pixel detector, which will be placed close to the beam-pipe and will measure the background rate in the area where the vertexing detectors will be installed. The target luminosity at

[2] Thermal neutrons are neutrons with kinetic energy below 0.025 eV [4].

the end of this phase is $1{\cdot}10^{34}\mathrm{cm}^{-2}\mathrm{s}^{-1}$ [6]. Another goal is to validate the simulation of beam induced backgrounds at the interaction region. The beams will be collided during this phase, which opens up the possibility of some physics measurements that do not require the vertexing detectors.

2.3.3 Phase 3

The full beam commissioning with the complete Belle II detector in place will be done at phase 3. Additional detector and accelerator tuning will be performed if necessary. After that, the main physics program of the experiment will start.

CHAPTER 3
The Belle II experiment

The Belle II experiment will be the highest luminosity B-factory to date, with integrated luminosity aimed at 50 ab^{-1} [1]. It will follow the successful operation of the Belle [8] and BaBar [9] experiments. By colliding electrons and positrons at the $\Upsilon(4S)$ resonance energy, $B\bar{B}$ mesons are copiously produced, since $\Upsilon(4S)$ decays to $B\bar{B}$ pairs with 96% branching fraction [4]. Belle and BaBar were the first experiments to detect the Charge-Parity symmetry (CP) violation in the B-meson sector [10] [11]. By analyzing an unprecedented amount of data from e^+e^- collisions, Belle II will continue the CP violation measurements, but its main focus will be the precision measurements of flavor physics reactions in the search for evidence of new physics, as in deviations from Standard Model predictions.

The Belle detector[1] will be upgraded to the Belle II detector, to match the new operating conditions of the SuperKEKB accelerator. The Belle II detectors is illustrated in Fig. 3–1, while the technical drawing of the detector is given in Fig. A–1. Belle II aims to retain the same performance as the Belle detector, but in an environment with much higher luminosity, and thus a higher background rate. Surrounding the interaction point, its task is to provide information about the particles created in e^+e^- collisions by measuring their energy, momentum, type, and trajectory. It consists of several sub-detectors described below.

[1] The coordinate system used for the Belle II detector is as follows: the origin is at the IP, x axis is horizontal and toward the outside of the accelerator tunnel, y axis is vertical upward, z coincides with the solenoid axis, which is bisector of two beams, towards the direction of electron beam; ϕ is azimuthal angle around z axis, with $\phi = 0$ defined for $(x, y, z) = (1, 0, 0)$, θ is the zenith angle with respect to z axis, with $\theta = 0$ defined for $(x, y, z) = (0, 0, 1)$.

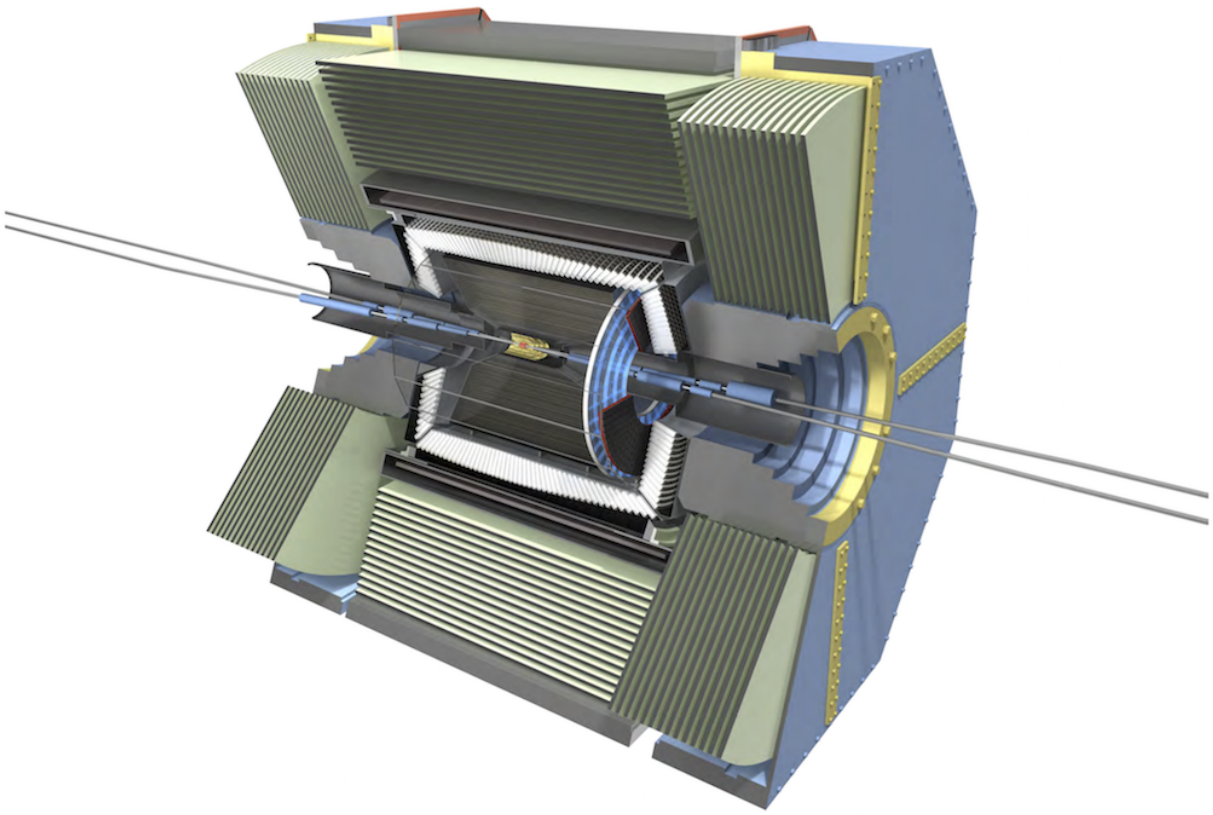

Figure 3–1: 3D model of the Belle II detector [12].

3.1 Pixel Vertex Detector

The Pixel Vertex Detector (PXD) is a new sub detector introduced in the upgrade from Belle to Belle II. It is located closest to the interaction region. Its purpose is to determine the B-meson decay vertex position. It consists of two layers of pixel detectors. The Depleted Field Effect Transistor (DEPFET) technology is used for detection of charged particles. As opposed to the Belle detector, a strip detector would not be able to perform precise B-meson decay vertex reconstruction because of the higher luminosity of SuperKEKB. The strip detector occupancy, that is the fraction of channels hit in each triggered event, would be too high at this distance from the interaction region. For that reason, the pixel sensors with higher numbers of channels were chosen. The concern was to avoid multiple scattering to keep the precise vertex reconstruction. The material budget was limited to 0.19% radiation lengths per layer. DEPFETs were chosen because of their small thickness and internal gain.

When a charged particle passes through the sensors, it creates electron-hole pairs in the depleted silicon. Due to the applied voltage bias, electrons drift towards the internal gate, creating a current. This current activates the transistor switch, signalling that a particle has passed through and the readout should be done. After the readout, the accumulated charges are cleared by a clear contact placed on the periphery of each pixel.

The inner layer is located at a radius of 14 mm, and the outer layer at 22 mm. The pixels are combined into ladders. The two layers contain 8 and 12 ladders, with pixel sizes of 50×50 μm^2 and 50×75 μm^2, respectively, with a total of 1600 channels. The

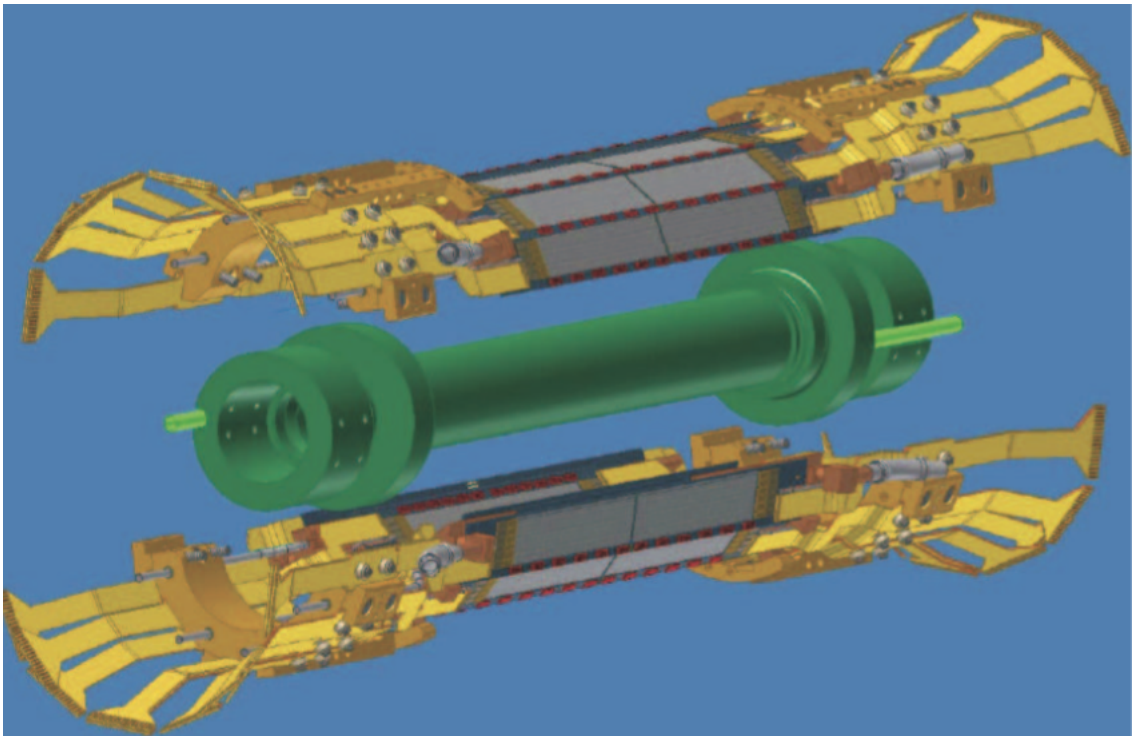

Figure 3–2: Support structure (shown in yellow) with PXD sensors mounted. Two half-shells are supported by the beam-pipe (shown in green) [1].

active area for the inner layer ladders is 80 mm long and 15 mm wide, while for the outer layer ladders it is 120 mm long and 15 mm wide. This matches the azimuthal detector acceptance between 17° and 150°. The readout and cooling mechanisms are located outside the acceptance region. A schematic of the PXD with its support structure is illustrated in Fig. 3–2. The readout time is 20 μs [13]. The amount of data recorded is reduced by combining the information from the Silicon Vertex Detector and keeping only the tracks that pass through both detectors. The spatial resolution is approximately 10 μm [1].

3.2 Silicon Vertex Detector

Together with the PXD, the Silicon Vertex Detector (SVD) forms the Belle II Vertex Detector (VXD). The SVD is located outside the PXD; its inner radius is 38 mm, and its outer radius is 140 mm [14]. It complements the PXD in the determination of the vertex position. The sensors are silicon strips organized into four layers. The layers are double-sided, with orthogonal strips on opposing sides. It covers the full angular acceptance of the Belle II detector, $17^\circ < \theta < 150^\circ$ [1]. This angular asymmetry was reflected in the design by introducing the partly slanted ladders to reduce the number of sensors and the amount of material particles typically pass through. The cooling mechanism and the support structure are located outside the acceptance region. To reduce the readout time, front end electronics needs to be placed as close as possible to the sensors, so the "Origami" chip-on-sensor technology was developed. Figure 3–3 shows a schematic of the SVD with one ladder shown for each layer.

There are three types of sensors. All are 300 μm thick [1]. The layer closest to the interaction region has the smallest rectangular sensors, 122.8×38.4 mm^2. The other three layers are made up of large rectangular sensors, 122.8×57.6 mm^2, with trapezoidal sensors, 122.8 mm length and width of 57.6 mm on the longer side, 38.4 mm on the shorter side, in the slanted region [14]. All the sensors are double-sided, the long strips of the p-side are parallel to and facing the beam axis. N-side short strips are orthogonal to the p-side strips, facing away from the beam axis, along the radial direction. The ladders are tilted to reduce the effect of deflection of electrons in the semiconductor due to the magnetic field which is parallel to the

beam axis.

In total, there are 172 double-sided silicon sensors, with a sensitive area of 1.13 m^2 and 223744 channels [14]. The predicted intrinsic resolution from the simulations performed is between 2 μm and 6 μm in the radial direction, and 10 μm to 30 μm in the z direction, depending on the position [1].

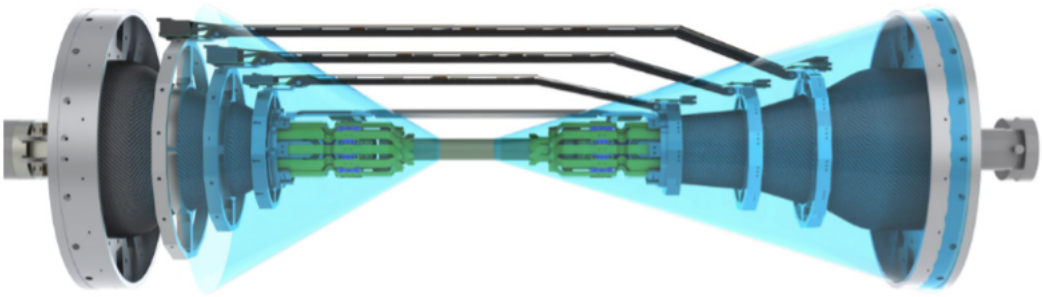

Figure 3–3: Schematic of the SVD [14]. Transparent cones indicate the borders of the active region. A single ladder is shown for each layer.

3.3 Central Drift Chamber

The Central Drift Chamber (CDC) in Belle II follows the same principles and uses the same material as Belle's drift chamber, with dimensions changed. It is used for the reconstruction of charged tracks and measurement of their momentum. Also, it can perform particle identification for the particles that do not reach the particle identification detectors by measuring their energy loss, and provides trigger signals for charged particles. CDC is a hollow cylinder with an inner radius of 160 mm and outer radius 1130 mm. The gas used is a mixture of 50% helium and 50% ethane, a mixture with low atomic number in order to reduce multiple scattering. Wires are parallel to the beam line. There are 14336 sense wires made of gold-plated

tungsten, 30 μm thick [1]. They are connected to a positive high voltage. Field wires are 126 μm thick aluminum ones, which are connected to the ground. Wires are organized into 56 layers and 9 superlayers to make tracking easier. A technical drawing of the CDC is shown in Fig. 3–4.

As a charged particle passes through the electric field in the CDC, it ionizes the gas. Its trajectory is curved because it is moving in the magnetic field of 1.5 T. The ionized electrons drift towards the anode sensing wires. Based on the magnitude of ionization per unit length and the trajectory in the magnetic field, a particle's charge and momentum and type are determined.

The measured spatial resolution of the CDC is 100 μm [1]. The resolution of energy loss per unit length, dE/dx, depends on the incident angle of the particle. The initial tests show it to be 8-12%.

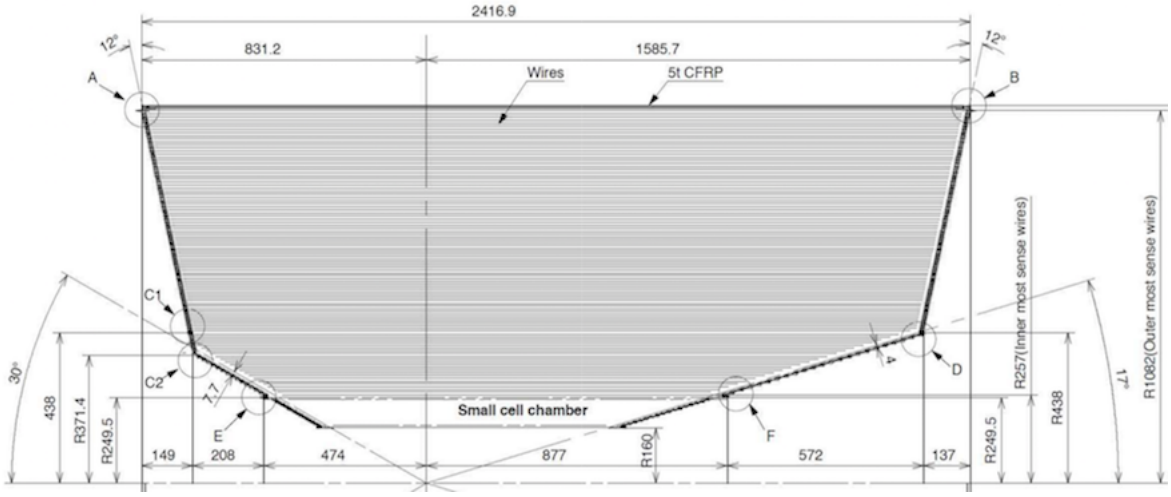

Figure 3–4: Schematic of the CDC [1].

3.4 Detectors for Particle Identification

Belle II Particle Identification (PID) consists of two detectors. The Time of Propagation (TOP) detector is used in the barrel region. The Aerogel Ring-Imaging Cherenkov Detector (ARICH) is used in the forward endcap region. Both are using the Cherenkov effect to detect the passage of charged particles. These detectors are designed to perform the identification of the particles with higher energies that could not be identified using the drift chamber, and especially to distinguish between $\pi^{\pm}$ and $K^{\pm}$.

If a charged particle passing through a medium has a speed larger than the speed of light in that medium, it will emit Cherenkov radiation. The emitted photons form a cone around the particle's trajectory. The opening angle of the cone is inversely proportional to the velocity of the particle,

$$\cos\theta_c = \frac{1}{\beta n},$$

where n is the refractive index of the medium and β is the particle's velocity as a fraction of the speed of light [4].

The TOP counter is made of 2.7 m long quartz radiators with a rectangular face, 45×2 cm^2. A focusing mirror is mounted on the forward-side face. The read-out micro-channel plate photomultiplier tubes (PMT) are located on the backward end. The quartz radiator's internal surface reflectance is 99.99%. The radiators are mounted on the outside of the CDC barrel, forming a cylinder with 16 radiators in total. Kaons and pions passing through the TOP counter generate the Cherenkov radiation which is totally internally reflected and read out by the PMT. Propagation

of the Cherenkov radiation in the TOP counter is illustrated in Fig. 3–5. By measuring the time from the electron-positron collision in the interaction region to the passage of the particle through TOP, and the spatial distribution of its Cherenkov radiation, it is possible to reconstruct the speed of the incident particle.

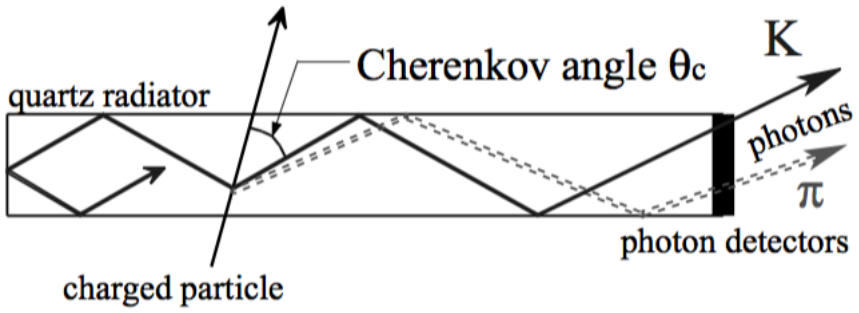

Figure 3–5: Side view of the inner reflection of the Cherenkov light inside the TOP counter [15].

The ARICH detector is made out of two-layer aerogel radiator tiles covering the forward endcap. Each of the layers is 20 mm thick and has a slightly different refractive index, as illustrated in Fig. 3–6. The readout is done by hybrid avalanche photodetectors, which are located behind the radiators, 20 cm away. As a charged particle passes through the aerogel radiator, it will emit Cherenkov radiation. The refractive indices were chosen such that the light coming from the two radiators will be focused on the photodetector plane. ARICH is expected to provide 4σ separation between pions and kaons up to momenta of 4 GeV/c, which is the energy limit of the experiment.

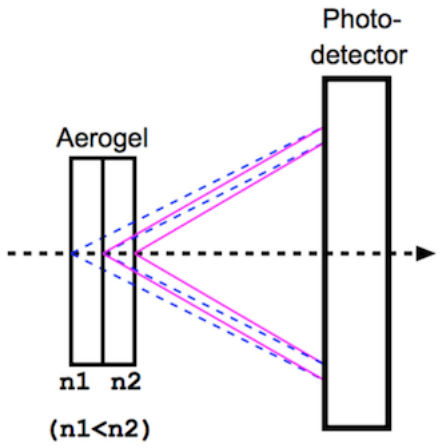

Figure 3–6: Principle of ARICH detection. Cherenkov photons (dashed blue and solid purple lines), emitted at different angles from the two radiators, are detected by the photo-detector [16].

3.5 Electromagnetic Calorimeter (ECL)

The electromagnetic calorimeter is used for measuring the energy of particles that interact through electromagnetic interaction, and for reconstruction of electrically neutral particles, such as photons and π^0's. It is made up of thallium doped caesium-iodide crystals that are organized into the barrel and forward and backward endcap. The crystals are truncated pyramids with the face 6.6 cm^2 on average. In total, there are 8736 crystals, 6624 in the barrel and 2112 in each endcap. They are read out using photodiodes with amplifiers. As a particle passes through the crystal, it interacts with the atoms in the crystal lattice and excites them, which in turn re-emit the absorbed energy in light form as they return to the ground state. The passing particle creates an electromagnetic shower. The crystals are big enough to contain the shower produced by electrons and photons, so the amount of light

emitted by the crystal is proportional to the energy of the incident particle.

Since Belle II will have a luminosity much higher than Belle, there is a concern for radiation damage of the ECL crystals. An upgrade to pure CsI for the endcaps is under consideration.

3.6 K_L^0 and μ detection (KLM)

The K_L^0 and μ detector (KLM) is the outermost detector of Belle II, located outside the superconducting solenoid. Its purpose is to detect muons and long lived neutral kaons. The muons are identified by combining the information from KLM with the track information from the CDC. K_L^0's, being neutral, do not leave any tracks in the CDC, and are reconstructed by combining the information from the ECL and the KLM.

The KLM is composed of alternating layers of 4.7 cm thick iron plates and active detector elements, glass-electrode Resistive Plate Chambers (RPC); the cross-section of an RPC is shown in Fig. 3–7. As a charged particle passes through the gas element of the RPC, it ionizes it. The high electric field causes electrons to cause more ionization, creating a streamer between the electrodes. The streamer is picked up by the readout strips on either side of the chamber.

An upgrade for endcaps is being considered. The simulations show that the RPC efficiency could dramatically fall in the Belle II environment due to high background rates. A use of scintillators to replace the RPCs is under consideration.

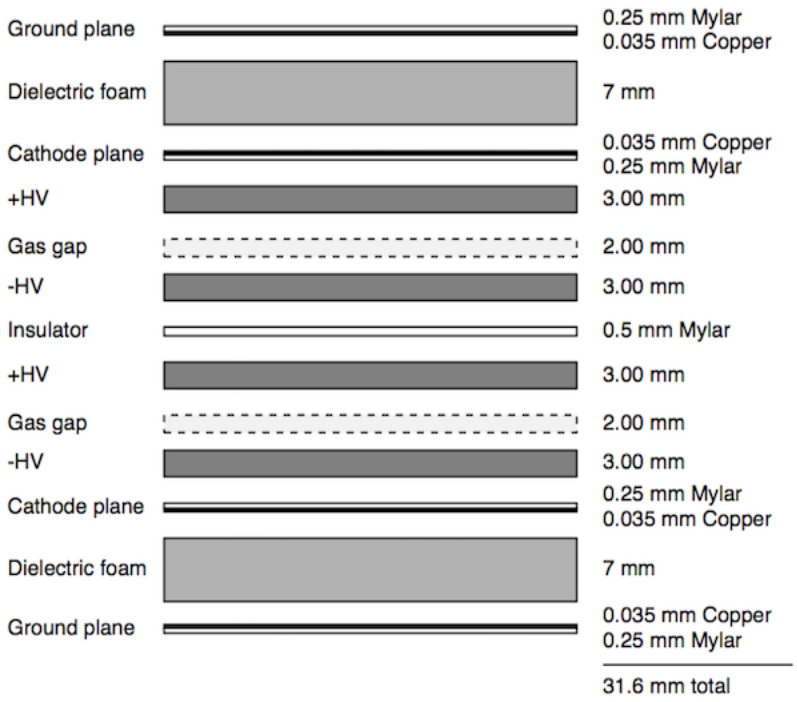

Figure 3–7: Cross-section of an RPC layer [1].

The Belle II detector is a particle spectrometer that was designed for performing high-precision physics measurements. With the new record-high luminosity design, the characteristics of the background environment in the detector are not well known. High background rates can deteriorate the detector's sensitivity and damage the detector itself. The previously described commissioning phases of the experiment (Chapter 2) are designed to provide information about the background rates that will be present in the detector, but a continuous monitoring of the detector environment during its operation is necessary. The most important sources of beam background are described in Chapter 4, while the subsequent chapters explain the design and simulation of such a background monitoring system.

CHAPTER 4
Background Sources at SuperKEKB

The effect of beam background on performance is one of the most important issues in the SuperKEKB and Belle II upgrade. Operating at 40 times higher luminosity than KEKB, the background rates are expected to increase 40 times [1]. This implies a higher beam-induced background rate in the Belle II detector. Different mechanisms govern the background radiation creation. Detector backgrounds arise from the following processes: interaction of beam particles with residual gas, Touschek scattering, synchrotron radiation, beam-beam interactions and operational particle losses due to beam injection and tuning. These processes will be explained, together with countermeasures employed at SuperKEKB and Belle II.

4.1 Beam-gas interactions

The operational vacuum pressure of SuperKEKB is 10^{-7} Pa on average [1]. Molecules of CO and H_2 are main constituents of the residual gas. The particles from the beams can interact with the remaining gas particles and thus their four-momentum is changed. These particles then hit the walls of the beam-pipe or the magnets. Shower particles are produced and constitute an important source of the beam-induced background at the Belle II detector. Fake hits that are generated by the shower particles deteriorate the detector resolution and the reconstruction of physics objects (*e.g.*, charged-particle tracks), and the accumulated radiation can cause damage to the detector.

The beam-gas interactions are electromagnetic interactions, with the two most important mechanisms being Coulomb scattering and Bremsstrahlung. The Feynman diagrams of these processes are shown in Fig. 4–1. The Coulomb interaction is a first order interaction, while Bremsstrahlung is an interaction at second order. Only interactions with residual gas nuclei are considered, since the interaction with the valence electron cloud is negligible compared to them. Deep inelastic scattering, where electrons from the beam break apart the gas nucleus, are not considered, since the cross-section is much smaller at the energies of SuperKEKB.

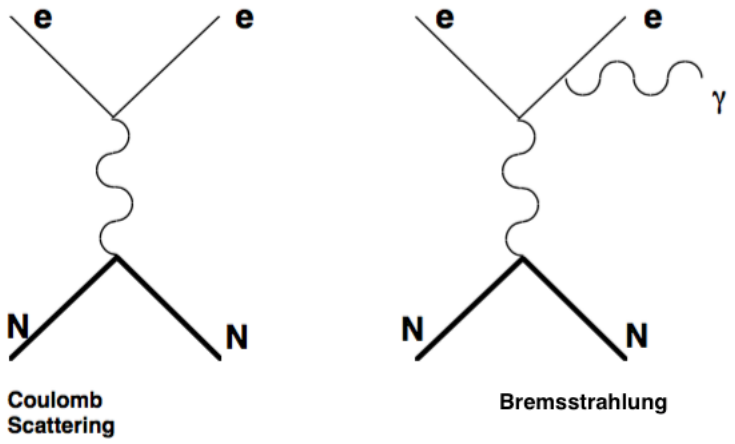

Figure 4–1: Feynman diagrams for Coulomb scattering (left) and Bremsstrahlung (right) [17]; N is a nucleus, while e can be either an electron or a positron.

4.1.1 Coulomb scattering

The Coulomb scattering can be classically approximated. The beam particles are elastically scattered by the residual gas nuclei, thus are no longer moving on the orbit, and are lost by hitting the inner wall of the beam-pipe. If an electron of velocity β and momentum $\vec{p}$ hits a nucleus of charge Z, the differential cross section

is given as [18][1]

$$\frac{d\sigma}{d\Omega} = \frac{Z^2\alpha^2}{4\beta^2|\vec{p}|^2\sin^4\frac{\theta}{2}},$$

where α is the fine structure constant and θ is the scattering angle of the electron. The total cross-section can be calculated from here. Using the high energy approximation, $\beta \approx 1$, $|\vec{p}| \approx E$, and the small angle approximation, $\sin\theta \approx \theta$, and avoiding the singularity that arises for $\theta = 0$ by introducing a minimum angle cut θ_c, the total cross-section is:

$$\begin{aligned}
\sigma_{Coulomb} &= \int_0^{4\pi} \frac{d\sigma}{d\Omega} d\Omega \\
&= \int_0^{2\pi} d\phi \int_{\theta_c}^{\pi} d\theta \sin\theta \frac{Z^2\alpha^2}{4\beta^2|\vec{p}|^2\sin^4\frac{\theta}{2}} \\
&= \int_{\theta_c}^{\pi} d\theta \frac{8\pi Z^2\alpha^2}{E^2\theta^3} \\
&\approx \frac{4\pi Z^2\alpha^2}{E^2}\frac{1}{\theta_c^2},
\end{aligned} \tag{4.1}$$

for $\theta_c << \pi$.

Since the Coulomb scattering rate is proportional to the vacuum level and the beam current, it was expected to have the same order of magnitude number of events in the new SuperKEKB environment, with the vacuum level being the same and the beam current increasing 2 times compared to the KEKB machine [1]. However,

[1] A natural system of units is being used, where $\hbar = c = 1$.

simulation studies have shown that the expected scattering rate is to be ~ 100 times higher compared to KEKB [19]. This is because of the changes introduced in the IR, a reduction of the beam-pipe radius from 35 mm to 13.5 mm [1]. The vacuum efficiency is reduced in the narrow pipes, thus this region will have a vacuum pressure higher than the rest of the accelerator.

4.1.2 Countermeasures against Coulomb background at SuperKEKB

In order to prevent the Coulomb-scattered particles from the ring reaching the detector, vertical collimators are installed upstream on both HER and LER rings. To stop the scattered particles, the aperture of these collimators should be smaller than or equal to the beam-pipe opening at the IR [19]:

$$\frac{d}{\sqrt{\epsilon\beta}} \leq \frac{r_{IR}}{\sqrt{\epsilon\beta}},$$

where d is the collimator width, β is the beta function and ϵ is the emittance of the ring. From here, the maximum collimator width is proportional to $\beta^{1/2}$.
Minimum collimator width is determined such as to avoid the Transverse Mode Coupling Instability (TMCI). As the particle bunch approaches the collimator, the leading particles create wake-fields that are proportional to their transverse displacement, which creates a collective force on the trailing particles. This creates a transverse oscillation of the tail particles, but this effect is stabilized due to synchrotron oscillations up to a threshold current [20]. From the condition of keeping the beam bunch current lower than the threshold, arises the expression for the minimum collimator width: $d_{min} \propto \beta^{2/3}$.

Given these conditions, the collimators should be located at a place along the ring where the beta function is small. It is determined that the allowed collimator width for LER is 2.23 mm $< d <$ 2.81 mm. The optimal position for installation is 82 m upstream of the IP. For the HER, the allowed width is 1.74 mm $< d <$ 2.26 mm at 61 m upstream of the IP [19].

4.1.3 Bremsstrahlung

Beam particles can be deflected by strong electric fields from the atomic nuclei of the residual gas. As the particles are accelerated by the electric field, they lose energy through emission of radiation, which is called Bremsstrahlung. If this energy loss is too large such that the particle energy error becomes larger than the storage ring energy acceptance, the particle is over-bent by the focusing magnets and hits the beam-pipe. The differential cross section for Bremsstrahlung is given by the Bethe-Heitler formula [17]:

$$\frac{d\sigma\left(Z,E,\epsilon\right)}{d\epsilon} = \frac{r_0^2 \alpha Z\left[Z+\xi\left(Z\right)\right]}{\epsilon}\Bigg\{\left[1+(1-\epsilon)^2\right]\left[\Phi_1(\delta)-F(Z)\right] - \frac{2}{3}(1-\epsilon)\left[\Phi_2(\delta)-F(Z)\right]\Bigg\},$$

where E is the energy of the incident electron, Z is the atomic number of the nucleus, ϵ is the fraction of energy carried away by the photon, and r_0 is the classical electron radius. The quantities Φ and f_c are the screening and Coulomb correction functions, respectively:

$$\delta = \frac{136 m_e}{Z^{1/3}E}\cdot\frac{\epsilon}{1-\epsilon}$$

$$\left.\begin{aligned}\Phi_1(\delta) &= 20.867 - 3.242\delta + 0.625\delta^2 \\ \Phi_2(\delta) &= 20.209 - 1.930\delta - 0.086\delta^2\end{aligned}\right\} \delta \leq 1$$

$$\Phi_1(\delta) = \Phi_2(\delta) = 21.12 - 4.184\ln(\delta + 0.952) \quad \text{for} \quad \delta > 1$$

$$F(Z) = \begin{cases} 4/3\ln(Z) & E < 0.05\text{GeV} \\ 4/3\ln(Z) + 4f_c(Z) & E \leq 0.05\text{GeV} \end{cases}$$

$$\xi(Z) = \frac{\ln(1440/Z^{2/3})}{\ln(183/Z^{1/3}) - f_c(Z)}$$

$$f_c(Z) = Z\alpha\left\{\frac{1}{1+Z\alpha} + 0.20206 - 0.0369Z\alpha + 0.0083(Z\alpha)^2 - 0.002(Z\alpha)^3\right\}.$$

Because Bremsstrahlung is a second order process, it has a smaller cross-section than Coulomb scattering, so it contributes less to the overall beam-gas background rate.

4.2 Touschek scattering

Touschek scattering is an intra-bunch scattering [21]. The beam particles are grouped into small bunches and they perform transverse, or betatron, and longitudinal, or synchrotron, oscillations. This increases the probability of elastic collisions between particles. The two particles emerge from the collision with changed energy and momentum, the small transverse momentum transformed into a large longitudinal momentum. If the new values fall outside the acceptance region for energy and momentum, the particles will hit the beam-pipe and be lost.

The Touschek effect should not be confused with intra-beam Coulomb scattering. The intra-beam scattering is a multiple scattering that leads to diffusion of the beam, while the Touschek scattering is a single scattering which leads to immediate loss of the colliding particles.

The particle loss rate due to Touschek scattering is defined by [2] [21]

$$\frac{dN}{dt} = -\frac{N}{\tau} = -R$$

and

$$R = \frac{1}{L_{circ}} \oint r \, ds,$$

where τ is the lifetime, L_{circ} is the circumference of the accelerator ring and r is the local loss rate. The local loss rate, Bruck's formula, is [2]

$$r(u_a, \varepsilon_x, \beta_x, \eta_x, \varepsilon_y, \beta_y) = \frac{r_e^2 c \beta_x N^2}{8\pi\gamma^3 \beta \sigma_{x\beta} \sigma_{y\beta} \sigma_z \sigma_x u_a} C(u_a), \tag{4.2}$$

where

$$C(u_a) = -\frac{3}{2} e^{-u_a} + \int_{u_a}^{\infty} \left(1 + \frac{3}{2}u_a + \frac{u_a}{2} \ln \frac{u}{u_a}\right) e^{-u} \frac{du}{u},$$

$$u_a = \left(\frac{\delta_a \beta_x}{\gamma \sigma_{x\beta}}\right)^2,$$

$$\sigma_x = \sqrt{(\epsilon_x \beta_x)^2 + \eta_x \sigma_\delta},$$

$$\sigma_{x\beta} = \sqrt{\varepsilon_x \beta_x} \quad \sigma_{y\beta} = \sqrt{\varepsilon_y \beta_y},$$

and δ_a is the momentum acceptance of the ring, $\sigma_{x\beta}$ and $\sigma_{y\beta}$ are transverse beam sizes determined; and $\gamma = \frac{E}{m_e c}$, where E is the beam energy and m_e is the electron mass. From here, it can be seen that the loss rate is inversely proportional to E^3 and to the beam size. The LER has a higher Touschek scattering rate than the HER. The energy asymmetry of the beams was reduced in part to reduce this rate. Due to the smaller beam size, it is expected that the Touschek background will increase by a factor of 20 compared to the KEKB [22].

4.2.1 Countermeasures against Touschek background at SuperKEKB

Movable collimators and heavy-metal shields are used to reduce the effect of the Touschek scattering. The heavy-metal shield is placed inside the detector, outside its acceptance region, between the beam-pipe and the inner detectors. An alloy of tungsten is used for the shielding; its radiation length being only 0.35 cm [4], it effectively stops the showers from reaching the inner detectors.

The movable horizontal collimators are installed on both inner and outer sides of both rings, at places where the beta function is large. There are 8 collimators for the LER and 11 for the HER, with their widths varying from 6.2 mm to 17.6 mm [22].

4.3 Synchrotron Radiation

As an electron travels through a magnetic field, it is accelerated and it emits radiation, which is called Synchrotron Radiation (SR). An electron with an energy $E = \gamma mc^2$ whose velocity forms an angle α with the magnetic field $\vec{B}$ spirals around the magnetic field line with angular frequency $\Omega = \frac{eB}{\gamma mc}$ [23]. The SR power is proportional to the beam energy squared and the magnetic field squared [24]. This indicates that the HER is the main source of SR at SuperKEKB since it has higher energy. The shape of the IR was modified to prevent SR from reaching the detector; ridge structures were added on the inner side of the beam-pipe to block the scattered photons from the IP [24]. The inner surface of the beryllium beam-pipe is gold-plated in order to absorb the synchrotron radiation. At KEKB, one focusing magnet was used on the downstream side, both for the final focusing of the LER beam and for the bending of the outgoing HER beam. This setup was a cause of significant SR reaching the Belle detector. At SuperKEKB, two separate magnets will be used, which will

significantly reduce the SR background. It is expected that the SR will not present a problem to the Belle II operation, as it is estimated that the SuperKEKB SR rate will be 800 times lower than that at KEKB [1].

4.4 Beam-beam interactions

The e^+e^- collisions that do not produce $B\bar{B}$ pairs, but involve other QED processes, also generate detector background. For Belle II, the most important types are the Radiative Bhabha (RBB) scattering and the wide-angle Bhabha scattering.

4.4.1 Radiative Bhabha interactions

The Feynman diagrams for the RBB scattering are shown in Fig. 4–2. The total cross-section is approximately

$$\sigma(\delta_a, \sigma_y^*) = \frac{16\alpha r_e^2}{3}\left\{\left(\log\frac{1}{\delta_a} - \frac{5}{8}\right)\left(\log\left(\frac{\sqrt{2}m_e\sigma_y^*}{\hbar c}\right) + \frac{\gamma_E}{2}\right) + \frac{1}{4}\left(\frac{13}{3}\log\frac{1}{\delta_a} - \frac{17}{6}\right)\right\},$$

where α is the fine structure constant, r_e is the electron radius, $\gamma_E = 0.577$ is Euler's constant, δ_a is the momentum acceptance of the ring, and σ_y^* is the beam cross-section at the IP [2].

Electron and positron energy is reduced by this scattering, so they are over-bent by the quadrupole magnets, creating showers when interacting with the magnet material. At SuperKEKB, the two separate quadrupole magnets are used for incoming and outgoing beams, so the orbits are centred in the magnets. It is expected that the showers from over-bent particles do not reach the detector, except in the case of large energy loss. The rate of RBB scattering is proportional to the luminosity, thus the rate is 40 times higher at SuperKEKB, compared to KEKB, but the effect is somewhat reduced due to the use of separate focusing magnets. The effect of the

electrons and positrons with large energy loss is still comparable to the Coulomb and Touschek background [24].

When photons generated in the RBB process reach the focusing magnets, they interact with the iron in the magnets and produce neutrons via the photo-nuclear resonance mechanism [24]. The neutrons produced by the photo-nuclear resonance have the biggest effect on the endcaps of the ECL and KLM [1]. Shielding is placed between the ECL endcaps and the beam-pipe to reduce the neutron flux. Each shield consists of a steel and a high-density polyethylene (HDPE) layer in order to reduce the radiation dose and the neutron flux in the ECL endcaps.

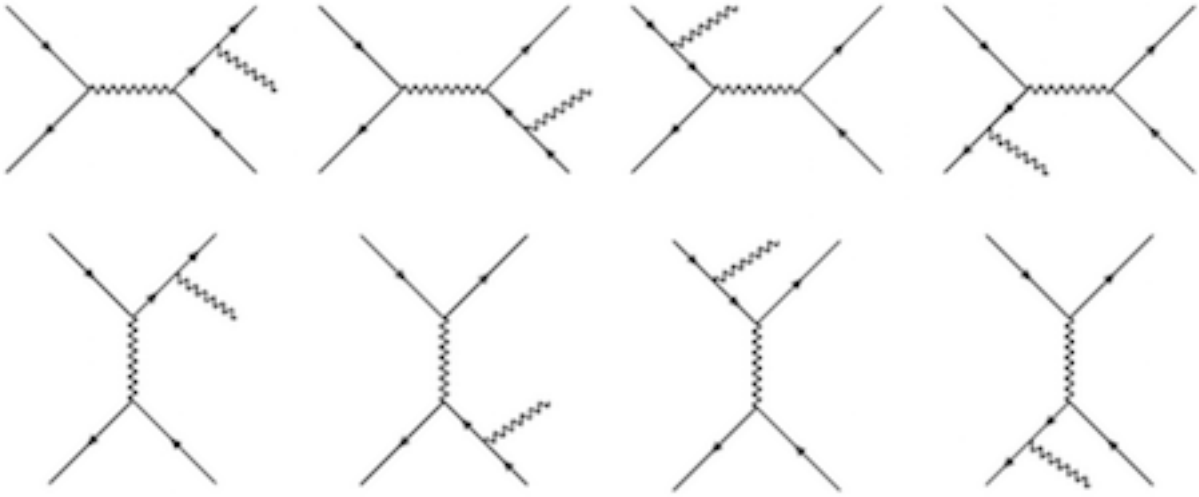

Figure 4–2: Full set of tree level diagrams for $e^+e^- \to e^+e^-\gamma$ [25].

4.4.2 Wide-angle Bhabha scattering

In most cases, electron-positron Bhabha scattering occurs in a way that the electron and positron do not change their energy or direction, and no photon emission occurs. Those events are not important from the aspect of beam background, since

it does not produce any interactions in the detector. Less frequently, the trajectories change so that both the particles, or one of them, reaches the detector. The "wide-angle" refers to the angle between the old and new trajectory being large enough so that the particle reaches the detector.

4.5 Injection background

The rate of previously mentioned background types is relatively easy to estimate from the simulation because the cross-section is known. For the background that arises from injection of new charge, it is hard to estimate the rate. The new background can arise from both the interaction of the newly injected charge with stored beam, and from SR due to tuning of the beam with magnets. This type of background has not been simulated. To get an estimate of the injection background rates, the measurements during phase 1 and phase 2 with the BEAST II detector will be performed.

A background environment that is higher than anticipated is dangerous for the detector, since it can degrade its resolution and damage its components. In addition to the commissioning phase of the Belle II experiment that is described in Chapter 2, the Belle II collaboration has developed a background simulation to analyze the expected background rates each sub-detector will be exposed to. During the detector's operation, monitoring of the background environment is crucial for its safe operation. A preliminary design of such a background monitoring system is described in Chapter 5.

CHAPTER 5
Beam Background Monitors

5.1 Performance requirements and initial design

It is important to have instantaneous feedback of the background particle environment in the Belle II detector so that the beam parameters can be optimized, for example by adjusting the collimator positions or tuning other accelerator parameters. Beam monitors that would provide such feedback for the Belle experiment are under construction. In particular, there is a need for such a monitoring subsystem to measure the background rate in the region of the ECL. Here, the design and simulation procedures for aspects of the beam background monitoring subsystem are explained.

Prior to Belle II, the original Belle detector had such background monitors. They were attached to the ECL endcap cylindrical steel shield, one on both forward and backward side, between the beam-pipe and the endcap. The detector consisted of a thallium-doped caesium-iodide scintillating crystal, which was read out by a photomultiplier tube (PMT). The PMT was read out using an oscilloscope, whose image was transmitted directly to the accelerator control room using a closed-circuit television camera. This setup was simple, but satisfied the need to provide the KEKB accelerator operators with instantaneous feedback on beam background conditions inside the Belle experiment.

Based on the background monitoring system used for Belle[1] , a similar system is under development for Belle II. The background monitoring detectors will provide quasi-instantaneous signals from the area near the ECL endcaps. The goal is to have the response speed fast enough to be able to observe and monitor the timing structures of SuperKEKB beam injection backgrounds, as well as the more slowly changing DC-like background rates.

The proposed position for the Belle II beam background monitors is inside the plastic (high-density polyethylene) part of the new ECL endcap shields, situated between the beam-pipe and the endcap. Based on the design used for Belle, a scintillation detector that consists of a PMT and a crystal is chosen as an initial proposal, but a design goal is to have a higher multiplicity of detection modules than what was implemented at Belle. To see if this is plausible in the new environment of SuperKEKB and to determine optimal positions and scintillator dimensions and geometries, a study of simulated ECL backgrounds was performed. This study is described in Chapter 6.

The beam-background monitoring system will need to be sensitive to the injection backgrounds discussed in Section 4.5. The two topped-up bunches are separated by 100 ns, so the timing resolution of the monitors would need to be better than 100 ns. A main goal is to provide information about the background rates, which implies that energy resolution is not a high priority. The system needs to be sensitive to a

[1] The information about the beam background monitoring project for the Belle experiment was obtained in private communication with the Belle II ECL group.

wide range of particle energies, so dynamic range is important. Most of the background types produce low-energy showers, but, for example, the Bhabha scatterings produce energetic hits, since the particle from the beam can directly interact with the detector. The background coming from the freshly injected bunches initially has a high energy, but as the bunches make several turns in the accelerator, it becomes less and less distinguishable. The monitors need to be sensitive to this damping of the injected beams, thus the need for a high dynamic energy range.

The signal from the background monitors will be provided to the SuperKEKB control operator. Using the provided signal, the control room operators will be able to fine-tune the beam parameters for optimal running conditions. Another possibility under consideration is to use this signal as a temporary veto for the Belle II data acquisition system in order to prevent radiation damage of the sensitive electronics during the periods of high background rates.

Given the requirements of the project and the previous experience from the Belle background monitoring project, it was decided to use a set of scintillation detectors for the background monitoring. The principles of operation of scintillation detectors are described in Section 5.2. The options considered for the choice of photodetector were a PMT, a conventional photodiode and an avalanche photodiode. The lifetime of a photodiode was found to be short in the high radiation environment of the Belle detector[2] . Given the even higher radiation environment expected in the Belle II

[2] Information obtained in private communication with the Belle II group from Université de Montréal.

detector, this option was quickly discarded. The avalanche photodiode (APD) has a high noise threshold of about 1 MeV. Given the energy depositions expected from the simulation results described in Chapters 6 and 7, this option was deemed unsuitable for the needs of the project. Thus, photodiodes and APDs were both excluded from further consideration.

5.2 Scintillation Detector Principles

Scintillators are materials that exhibit a characteristic known as luminescence. When excited by ionizing radiation, they re-emit the absorbed energy in the form of light. This phenomenon is used for particle detection. A scintillating material is coupled to a light detector for readout. Scintillating crystals and photomultipliers, the most widely used photo detectors, are described in the following sub-sections.

5.2.1 Scintillators

As a particle passes through the scintillator, it deposits energy via ionization. This excites the atoms of the crystal, which radiate scintillation photons as they return to their ground states. The scintillation decay time is the time it takes to emit 63% of the scintillation light after the energy deposition. The light yield is the number of scintillation photons emitted per unit of energy deposited. The radiation length of a scintillator, X_0, is the thickness of the material needed so that a passing electron loses all but $\frac{1}{e}$ of its energy.

Scintillators are divided into two large groups, organic and inorganic scintillators. Organic scintillators have fast decay time and high light yield, but the light yield is not linear with energy deposited. They are of relatively low density, averaging 1 g/cm^3. They are available in a variety of shapes and sizes, in liquid and solid form.

Because of this, they are widely used in particle detectors and X-ray detectors, when there is need for accurate timing measurement. Inorganic scintillators have higher density than organic, slower decay time, lower light yield, but better linearity. They are often used in calorimeters, to measure the energy deposition of a particle.

5.2.2 Photomultiplier

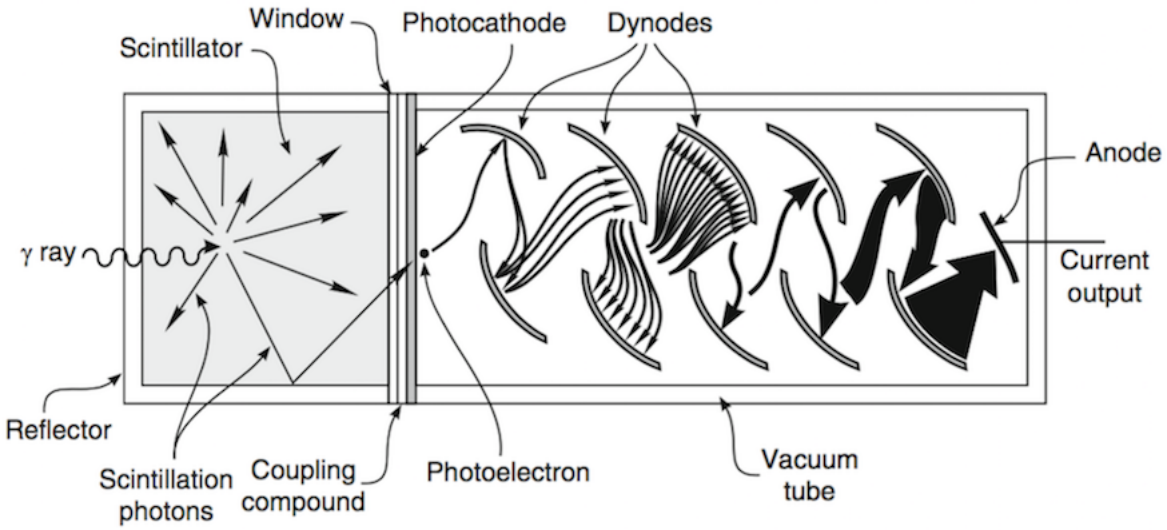

Figure 5–1: The principle of operation of a scintillation detector [26]. An incoming γ ray was used for the example; the γ interacts with the scintillator, which in turn emits scintillation photons; when the photons reach the photocathode of the PMT, a photoelectron is emitted, and releases more electrons as it reaches the dynodes; this produces the output current.

A photomultiplier tube (PMT) is commonly used to collect the light produced by a scintillator and convert it to a measurable voltage pulse. The operation mechanism of a PMT is shown in Fig. 5–1. Photocathodes are made from a material with a suitably low work function. Depending on the material choice for the photocathode, the sensitive wavelength range of the PMT is determined. As a photon

strikes the photocathode, it produces a photoelectron by way of the photoelectric effect. The probability that the incident photon generates a photoelectron is called the quantum efficiency of the PMT. The photoelectron is accelerated by the electric field towards the next electrode (dynode). Each dynode is coated with a material suitable for high secondary emission, and it is held at a high voltage compared with that for neighbouring dynodes, creating a high electric field. Several electrons are produced when the photoelectron hits the first dynode. All these electrons are then accelerated towards the next dynode, which in turn produces more electrons. This electron multiplication process is repeated in several stages. Generated electrons are collected at the anode. The number of electrons collected for every generated photoelectron is called the gain (G) of the PMT.
The operation of a PMT is affected if it is placed in a magnetic field. The magnetic field bends the electrons, so that they do not hit the dynodes. This effect is pronounced in models with a long path length from photocathode to the first dynode. By using dynodes with a fine mesh structure, this effect can be somewhat reduced.

Using scintillation detectors in the background-monitoring project is the best option, since they match the requirements of the project, and were already successfully used for the same purpose in the Belle era. The next step in the design is choosing a suitable scintillation material, a PMT model and the optimal azimuthal positions in the ECL shields. The ECL background simulation was used to get an idea of the background environment these detectors will be placed in, which facilitated the

decision making. The analysis of the ECL background simulation is described in Chapter 6.

CHAPTER 6
Simulation of the ECL background

To determine the optimal positions of the background monitors, a study of the simulated background visible to the ECL was performed. The background simulation was a joint effort of the SuperKEKB and Belle II collaborations. Here, the examined background types are Coulomb, Touschek, Radiative Bhabha and wide angle Bhabha. These background types are described in Chapter 4. For Coulomb and Touschek samples, particles were tracked along each location in the whole ring using the Strategic Accelerator Design (SAD) simulation [27]. BB-BREM [28] and BHWide [29] generators were used to simulate the Bhabha scattering. These were used as input for a GEANT4 [30] simulation of the Belle II detector, where the detector response was recorded. The simulation was executed in the basf2[1] framework and the results were analyzed using ROOT software [31].

The SAD software was developed at KEK in 1986 for the purpose of accelerator design [27]. It provides particle tracking along the high and low-energy rings. The particle momentum and location of particle loss are used as an input for the Geant4 simulation of the Belle II detector to simulate the effect these lost particles have on the detector.

[1] The basf2 framework software was developed by the Belle II collaboration for the online and offline data handling.

The BB-BREM [28] generator was used to simulate the radiative Bhabha scattering, $e^+e^- \to e^+e^-\gamma$. It uses a Monte Carlo algorithm to generate random events in phase space. The distribution of the events closely matches the cross section for this interaction. Each generated event is a complete description of the momenta of produced particles, on which experimental cuts can be imposed.

The BHWide generator is a wide-angle($\theta > 6^\circ$) [32] Bhabha event generator. It was first developed for the LEP1 and LEP2 experiments [29]. It calculates the cross-section based on the Yennie-Frautschi-Suura exponentiation [33], which is realized via a Monte Carlo algorithm. The input parameters are the center of mass energy and other relevant cuts on the outgoing particles.

		Forward Endcap	Barrel	Backward Endcap
Coulomb	LER	34.3±0.4	1053±6	394±3
	HER	1.51±0.09	7.6±0.3	2.74±0.13
Touschek	LER	33.3±0.4	480±5	234±3
	HER	24.2±0.5	35.1±0.5	103.0±1.2
RBB	LER	7.49±0.14	252.5±1.1	160.4±1.1
	HER	124±3	275.8±1.3	12.68±0.18
BHWide	LER	68.0±0.6	2599±13	1910±40
	HER	670±40	2270±30	93±1

Table 6–1: Energy deposited [GeV] per 1 ms by each background type in the ECL detector endcaps and barrel for the low-energy (LER) and high-energy (HER) rings, respectively, with one standard deviation of uncertainty indicated due to simulated samples sizes only.

The total energy deposited per millisecond by each background type in the ECL detector is given in Table 6–1. The statistical uncertainty is cited as one standard deviation. It is obtained by the bootstrap resampling method [34]. The

total energy is calculated as a sum of energies of individual shower deposits. Since the underlying distribution of the individual shower energies is unknown, the sample was used to generate populations by randomly selecting the values from the sample. The values were chosen using the random generator available in ROOT software, TRandom [31]. After the selection, each data point was returned to the sampling pool, so it could be chosen more than once. After creating a new population, the total energy was calculated. This process was iterated 2000 times. The total energy distribution converged to a Gaussian, from which the mean and sigma were obtained. With no knowledge of the underlying distribution and the systematic uncertainties of the simulation, this process provided the statistical uncertainty for the total energy deposited by each background type.

The spatial distribution of energy hits is shown in figures 6–1, 6–3, 6–4, 6–5.

6.1 Coulomb background

The spatial distribution of Coulomb type background energy deposits in the ECL is shown is Fig. 6–1. Since the cross section for Coulomb scattering is inversely proportional to energy squared, as shown in Equation 4.1, it is expected to see more scatterings in the low energy beam. It can be seen from Table 6–1 that the Coulomb LER type of background deposits more energy than the HER. In Fig. 6–2, a histogram of the simulated location of primary vertices is plotted. The primary vertex location is the location at which the particle is lost from the beam by hitting the beam-pipe. For the electron beam, all the simulated vertices are located at -122.7 cm on the z-axis. This is the case because this position was hand-calculated; it is not tracked by SAD. This position is close to the backward endcap, so all the energy deposition

is in the backward endcap and in the barrel close to the backward endcap. The forward endcap receives a much smaller energy deposition. The Coulomb scattering of the LER is tracked by SAD, and the distribution of the primary vertices is plotted in Fig. 6–2. The majority of the particles are lost after passing the forward endcap, around the point where the beam-pipe is getting narrower. As these particles are directed in the negative z direction, the net momentum of the shower they create retains the same direction. These showers are detected mostly in the backward endcap, in the crystals closest to the beam-pipe, with a small part of the shower reaching the forward endcap. Another place where the particles are lost is at the point where the beam-pipe becomes wider, after the IP, close to the backward endcap. The showers generated from these particles deposit energy primarily in the backward endcap, again in the crystals closest to the beam-pipe.

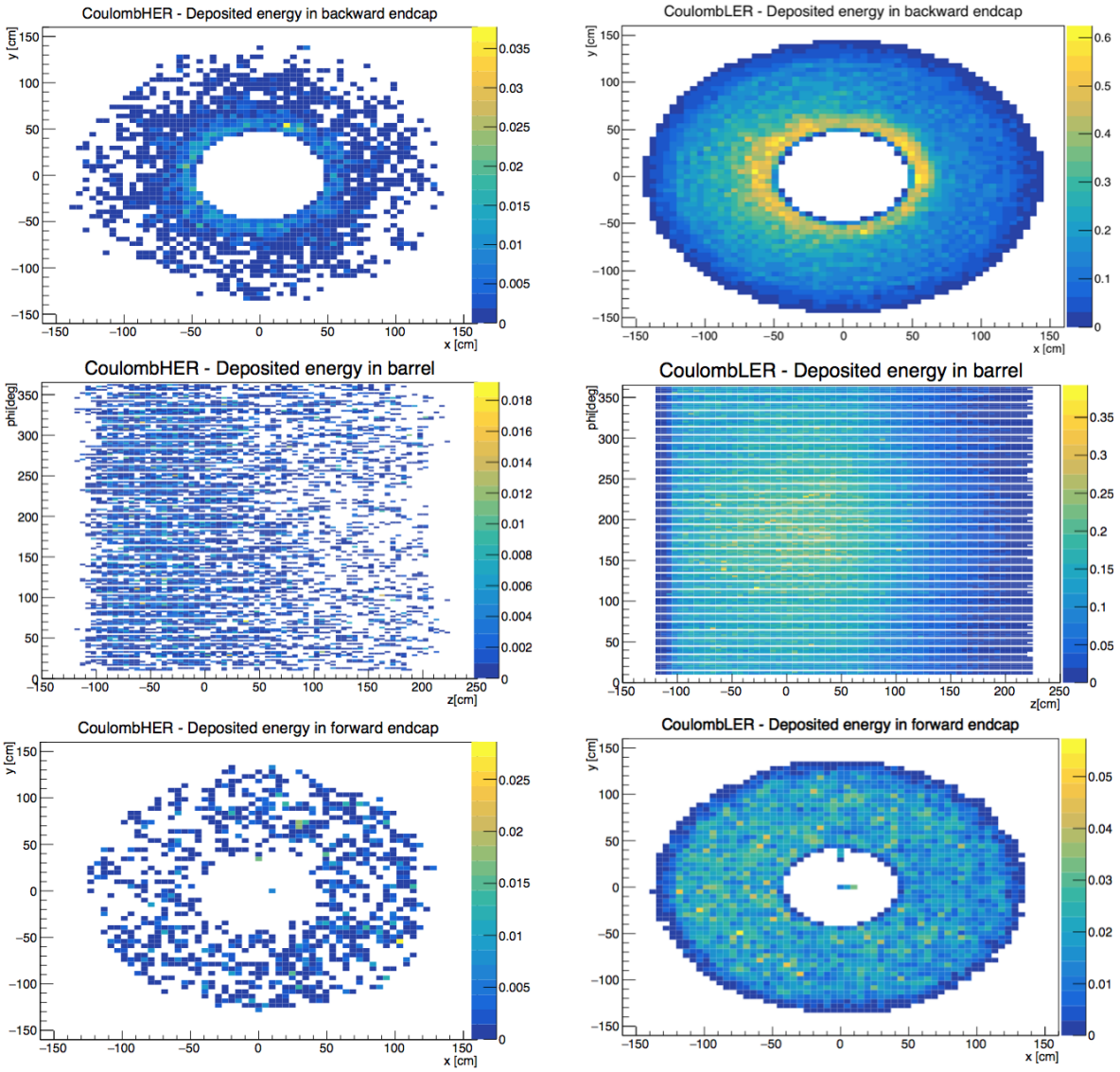

Figure 6–1: Spatial distribution of energy deposition for the Coulomb scattered background. The plots on the left are for the high-energy beam, while the plots for the low-energy beam are on the right. The top row shows the energy deposition in the backward endcap, the plots in the middle show the barrel, and the plots on the bottom show the forward endcap.

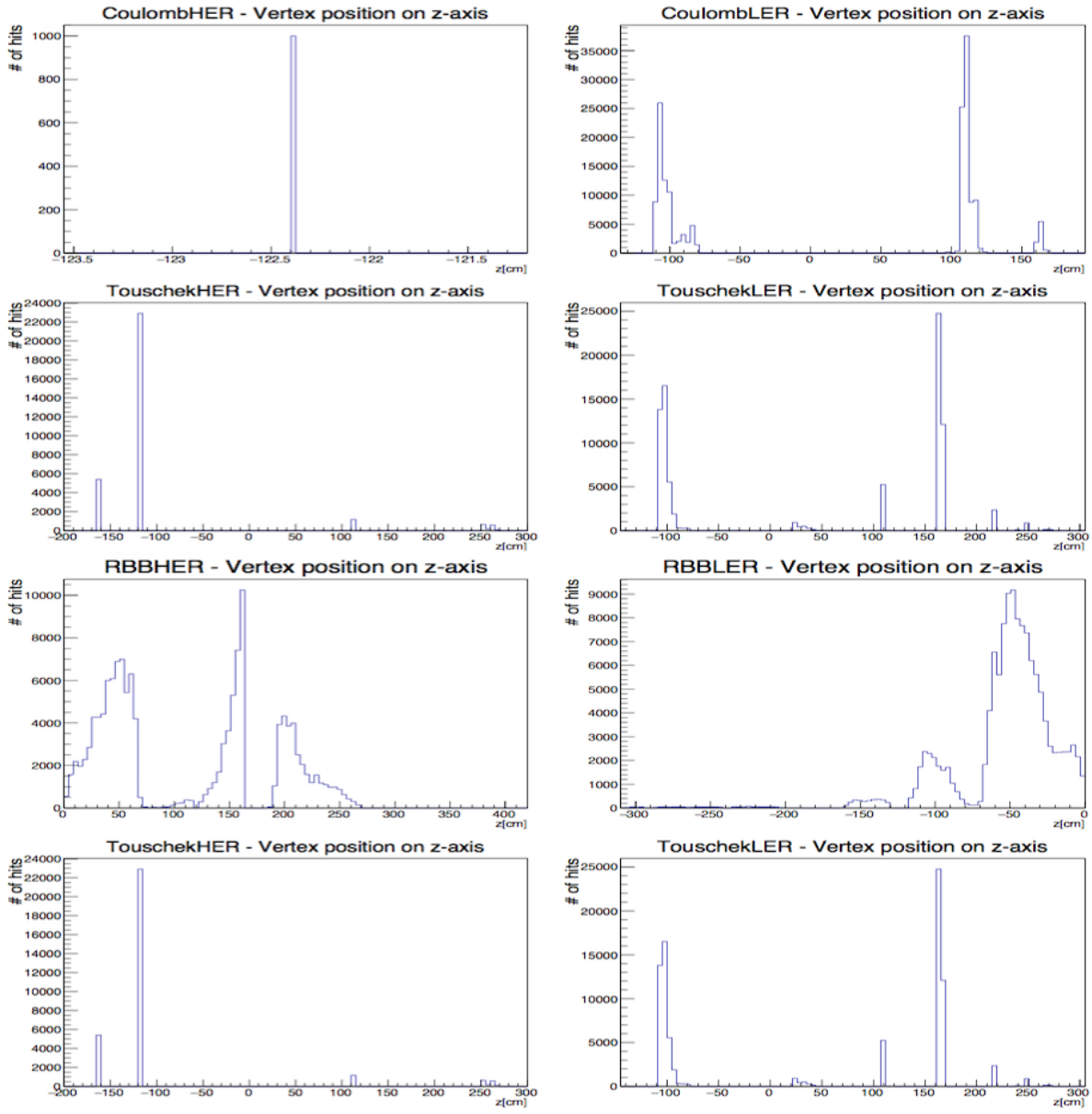

Figure 6–2: Simulated z-axis position of the initial hit in the beam-pipe for each background type. The plots on the left show the high-energy beam primary vertices; the plots on the right show the low-energy beam vertices. The z-position of the hit is shown on the x-axis; the y-axis shows the total number of hits in the corresponding location.

6.2 Touschek background

Figure 6–3 shows the spatial distribution of energy deposition in the ECL resulting from the Touschek scattering. Figure 6–2 shows the z-position of the primary vertices. Since the cross section for Touschek scattering is proportional to E^{-3}, the low energy beam has a higher particle loss due to this effect. The effect of Touschek scattering is greatly reduced by implementing the countermeasures described in Subsection 4.2.1. For the high energy beam, the losses with the most significant impact on the ECL are the ones lost before reaching the IP. The energy deposition is concentrated in the backward endcap, in the crystals closest to the beam-pipe. The particle loss in the low energy beam is dominant both before and after the IP. The energy deposition pattern is similar in the backward and forward endcaps. There is a hot spot in the forward endcap at the ϕ =180° position. This is because the LER is located closest to this position of the endcap. Similarly, after the HER and LER beam cross at the IP, the hot spot in the backward endcap is at the ϕ =0° position, where the beam-pipe is the closest.

6.3 Radiative Bhabha background

The location of simulated primary vertices for radiative Bhabha scattering is shown in Fig. 6–2. Since the scattering occurs at the IP, the particle loss for the high energy beam happens at positive z positions, and for the low energy beam it happens at negative z positions. Thus, as seen in Fig. 6–4, the energy deposition from the HER occurs mostly in the forward endcap and the part of the barrel close to it. For the LER, the energy is deposited primarily in the backward endcap and at the barrel, in the region near the backward endcap.

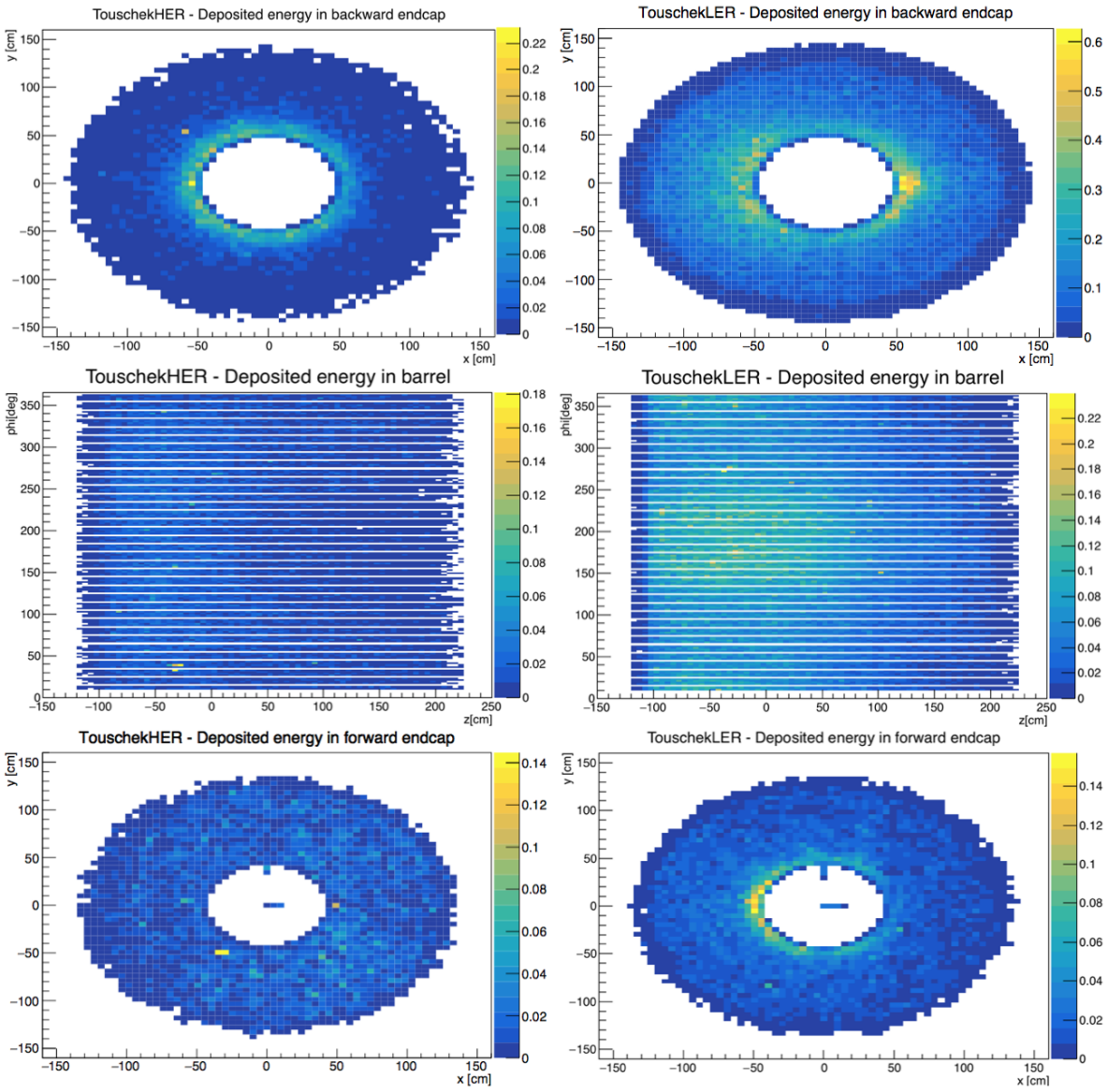

Figure 6–3: Spatial distribution of energy deposition for the Touschek scattered background. The plots on the left are for the high-energy beam, while the plots for the low-energy beam are on the right. The top row shows the energy deposition in the backward endcap, the plots in the middle show the barrel, and the plots on the bottom show the forward endcap.

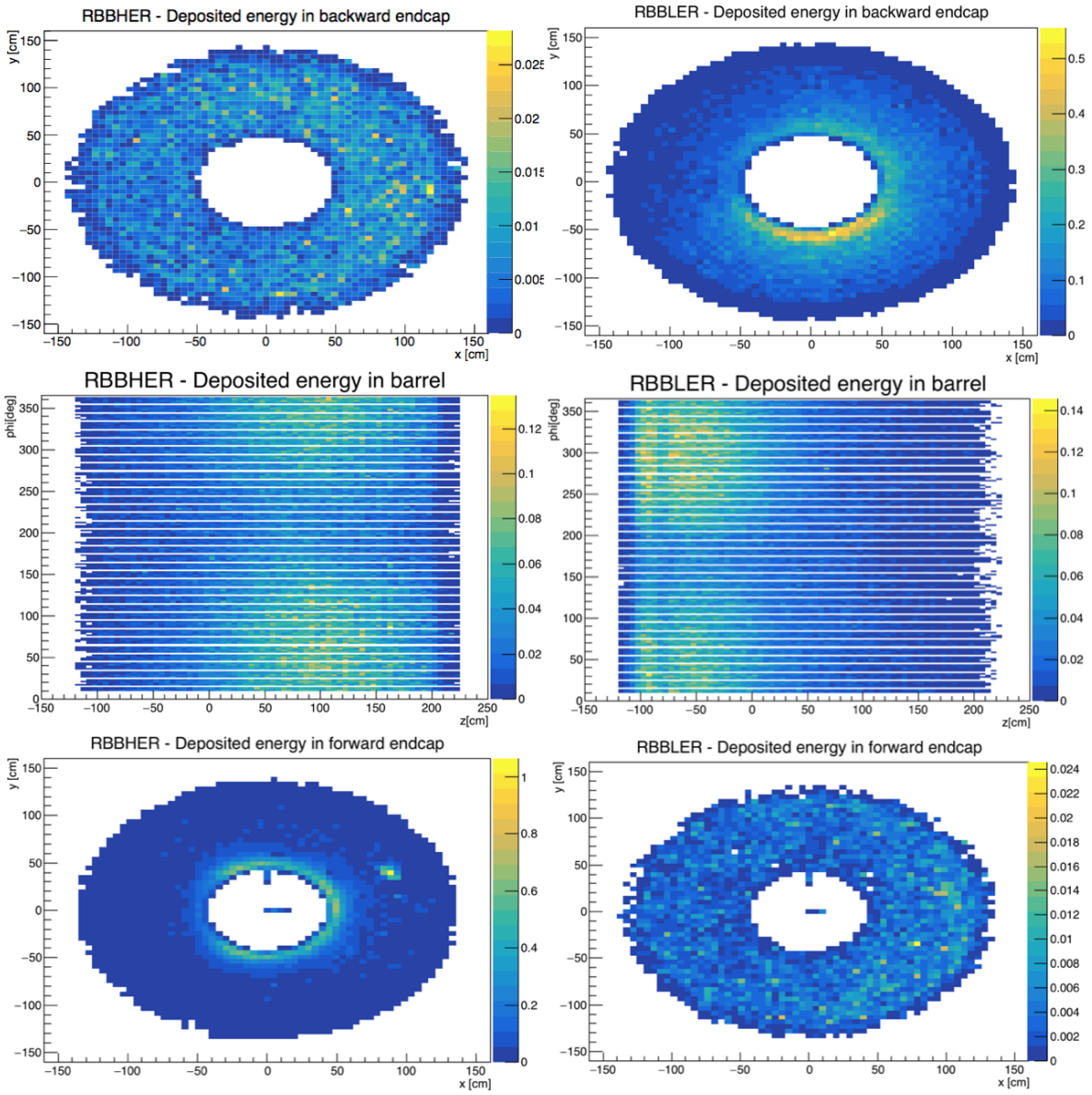

Figure 6–4: Spatial distribution of energy deposition for the radiative Bhabha scattered background. The plots on the left are for the high-energy beam, while the plots for the low-energy beam are on the right. The top row shows the energy deposition in the backward endcap, the plots in the middle show the barrel, and the plots on the bottom show the forward endcap.

6.4 Wide-angle Bhabha scattering

As previously described in Chapter 4, the wide-angle Bhabha scattering is when the electron and positron interact such that the momentum after the collision is changed such that both the particles, or one of them, are deflected from the beam into the detector. This is why this type of background deposits large amounts of energy. From Fig. 6–5, it can be seen that these hits in the ECL have distinct hot spots, in the forward endcap for the HER, and in the backward endcap for the LER. This is because the electron or positron from the beam enter the detector immediately after scattering, rather than hitting the beam-pipe or some shielding and starting the shower there, which then propagates through the detector. This is why this type of background can be potentially damaging to the detector. The electron/positron hits can be falsely interpreted as a physics event originating at the nominal interaction point, which would lead to degradation of detector performance.

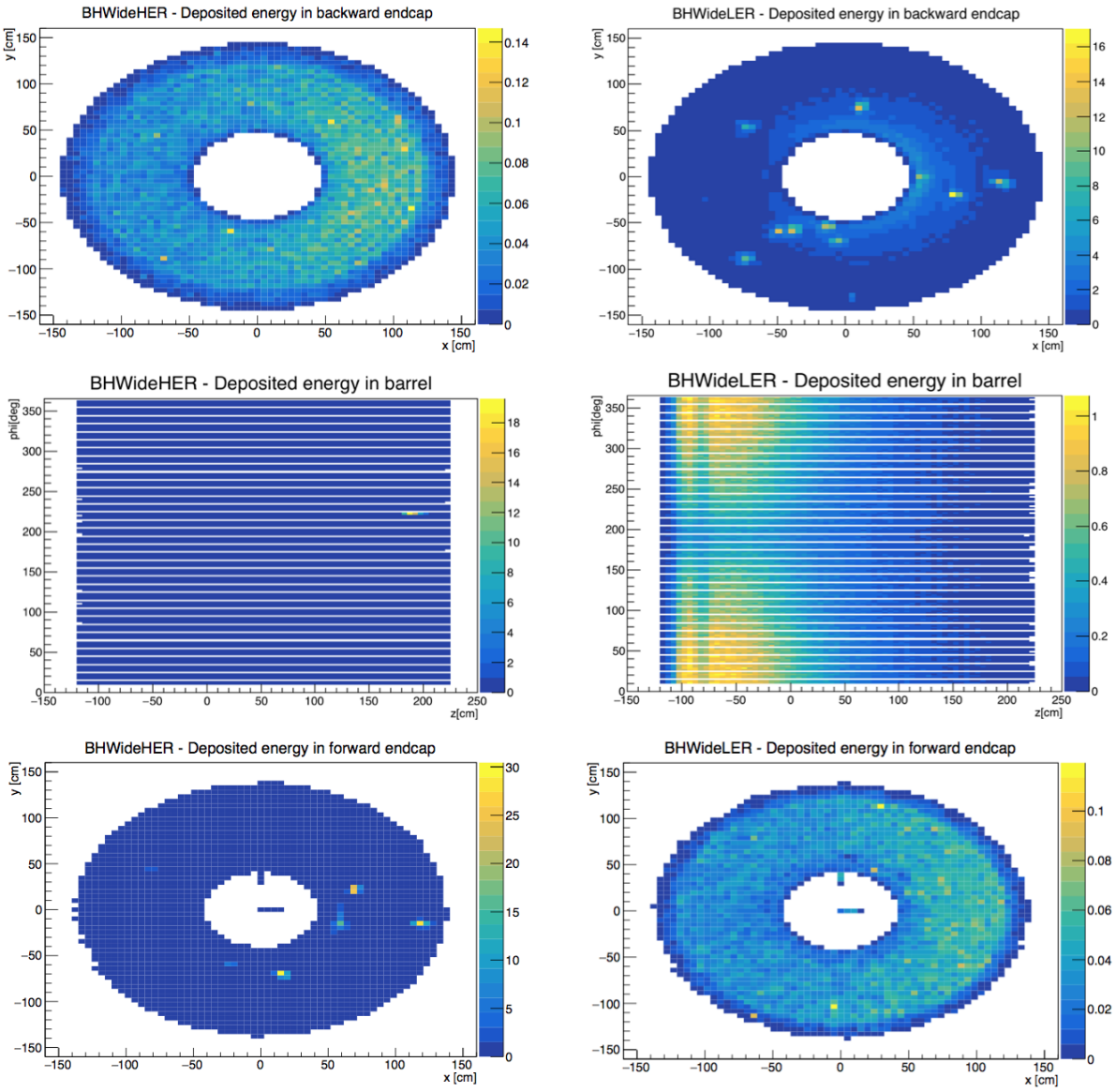

Figure 6–5: Spatial distribution of energy deposition for the wide-angle Bhabha scattered background. The plots on the left are for the high-energy beam, while the plots for the low-energy beam are on the right. The top row shows the energy deposition in the backward endcap, the plots in the middle show the barrel, and the plots on the bottom show the forward endcap.

6.5 Placement of the background monitors

Based on the background simulation results for the ECL, the position of the background monitors was chosen. The decision to place the background monitors in the polyethylene part of the shields was already made, but not the azimuthal position. Based on the spatial distribution of energy deposition in the ECL endcaps, the hits were evenly distributed around ϕ. It was chosen to have four detectors on each forward and backward side, placed at $\phi = \{0°, 90°, 180°, 270°\}$.

The energy the background monitors would receive was initially approximated by looking at the crystals from the ECL endcaps closest to the positions of the monitors. The crystals at the positions $\phi = \{0°, 90°, 180°, 270°\}$ of the innermost ring of the forward and backward endcap were chosen. Fig. 6–6 shows the energy deposition per 1 ms per cm^3. The results of the Coulomb, Touschek, radiative Bhabha and wide-angle Bhabha simulations were added up to get the total energy deposited. All the simulation results were obtained for the 1 ms interval, which facilitated the addition. The total amount of energy deposited was divided by 1080 cm^3, the average volume of the ECL crystal, to obtain the energy deposited per cm^3. These results show that the energy deposition per 1 ms per 1 cm^3 is relatively low, on the order of 5 MeV on average. To be able to monitor the background rate, the chosen scintillator needs to have a large enough volume so that the particles passing through would interact with the atoms in the crystal lattice. The radiation length of the chosen crystal should be short enough for the passing particles to deposit enough energy to produce a distinguishable signal. The choice of the crystal is described in Chapter 7.

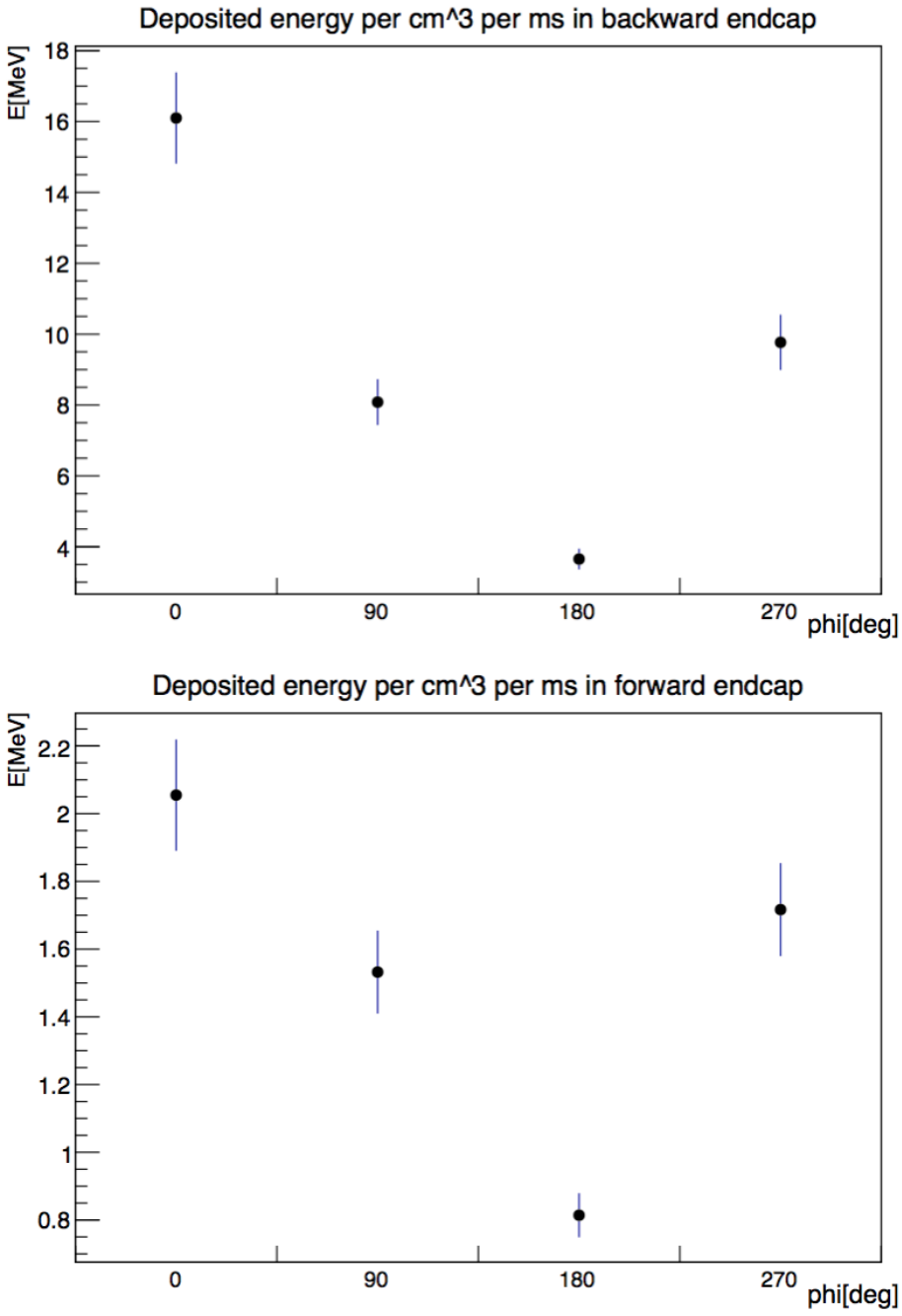

Figure 6–6: Energy deposited [MeV] per 1 ms per 1 cm^3 in the crystals closest to the positions of the background monitors.

CHAPTER 7
Beam Background Monitors: Simulation and Final Design

Based on the results from the ECL background simulation, a choice for the background monitor azimuthal positions and scintillator material was made. The biggest constraint on the detector was that it needed to fit in cylindrical holes drilled in the polyethylene part of the ECL endcap shield. The design of the shield only allowed a hole diameter of 42.7 mm and depth of 100 mm, in the direction parallel to the z-axis. The chosen positions at $\phi = \{0°, 90°, 180°, 270°\}$ were not available because this position was already occupied by the bolts that keep the two parts of polyethylene in place. Because of this, the ϕ positions were offset by 4°, so the design positions became $\phi = \{356°, 86°, 176°, 266°\}$.

7.1 Scintillator and photomultiplier technology selection

The two crystals taken into consideration were lutetium-yttrium oxyorthosilicate (LYSO) and thallium doped caesium-iodide (CsI(Tl)). The LYSO crystal was chosen as an attractive option because of its high density, high light yield, and short decay time. The CsI(Tl) crystals were readily available because they were already used in the calorimeter [1]. The characteristics of the two types of crystals are listed in Table 7–1.

Even though LYSO has lower light yield than CsI(Tl), its other characteristics are better suited for the intended use. The light yield is still high enough to provide a good signal-to-noise ratio. Concerning the rate measurements, the decay time of

	CsI(Tl)	LYSO
Density(g/cm^3)	4.51	7.10
Radiation length(cm)	1.86	1.14
Decay time(ns)	1220	40
Wavelength of emission maximum(nm)	550	420
Light yield(photon/MeV)	54000	32000
Hygroscopic	slightly	no

Table 7–1: Comparison between the characteristics of LYSO and CsI(Tl) crystals [4].

40 ns is short enough to distinguish between two injected bunches, which are spaced at 100 ns. LYSO features excellent radiation hardness [35], which is required in the high background-rate environment. The background monitors at Belle suffered great radiation damage[1] . The short radiation length and high density of LYSO allows for crystals small enough to fit the predefined holes in the polyethylene layer of the shields. Because of these advantages of LYSO over CsI(Tl), LYSO was chosen for the scintillator for the background monitors.

The LYSO crystal is naturally radioactive, because of the radioactivity of the lutetium isotope ^{176}Lu (abundance of 2.6%), with a half-life of $3.6{\cdot}10^{10}$ year [36]. It decays to ^{176}Hf via a beta decay followed by three simultaneous γ-ray emissions. The decay scheme is shown in Fig. 7–1. The intrinsic radiation of the LYSO crystal is not a problem for this implementation since the energies that it emits are lower than the typical background shower energy. The natural radioactivity of the LYSO will have an impact on the energy resolution of the background monitors, which is not an issue

[1] The information about the beam background monitoring project for the Belle experiment was obtained in private communication with the Belle II ECL group.

for this use, as discussed in Chapter 5.

There were a couple of considerations that had to be taken into account when choos-

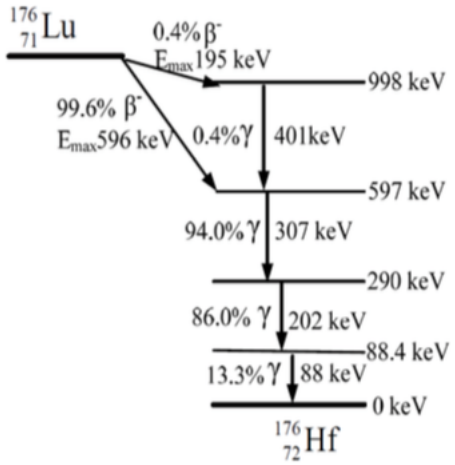

Figure 7–1: Decay scheme of ^{176}Lu [37].

ing the photomultiplier tube to be used for the background monitoring project. The biggest constraint is that the area where the monitors are to be installed is inside a high magnetic field. The information about the magnetic field values at the relevant positions was obtained from the Belle II B-field group. A set of measurements of the magnetic field was performed earlier this year, but the measurements were coarse in the area of interest ($dz \cdot dr \cdot d\phi = 4\text{cm}\cdot 4\text{cm}\cdot 2°$). The values were extrapolated to get the B-field information at 9 positions for each recess, at the 3 positions on the face of the recess, 3 positions in the middle of the recess and 3 positions in the end of the recess. For the backward endcap, the values are constant at all the positions, at 1.5 T in the z-direction. For the forward endcap, the values at the positions closest to the beam-pipe are 1 T; at the positions in the middle of the hole and at the positions furthest away from the beam-pipe, the B-field is 2.1 T in the z-direction.

A conventional PMT would not work in such a high magnetic field environment. Hamamatsu produces a range of PMTs for operation in high magnetic fields. Model R7761-70 best matches the needs of this project. Its characteristics are outlined in Table 7–2. The PMT model R7761-70 uses the fine-mesh dynodes to combat the sensitivity to the magnetic field. The mesh-type PMTs have a structure of fine mesh electrodes that are stacked in close proximity. There are 19 dynodes in total, with a mesh width of 13 μm. Having the dynodes at close proximity reduces the length the electrons have to travel, so their deflection by the magnetic field is less prominent.

PMT Hamamatsu R7761-70	
Tube diamater(mm)	38
Diameter of effective area(mm)	27
Spectral response range(nm)	300 to 650
Peak wavelength(nm)	420
Photocathode material	bialkali
Dynode stages	19
Gain at 0 T	$1.0{\cdot}10^7$
Gain at 1.5 T	$1.0{\cdot}10^4$

Table 7–2: Properties of PMT R7761-70 [38].

The photomultiplier and the crystal need to fit in the pre-manufactured recess in the shield. The PMT length is 63 mm, plus the needed length of the leads. This leaves room to have a 30 mm long crystal. The diameter of the active area on the front of the PMT is 27 mm. Based on that, it was chosen to have a cylindrical crystal with a diameter of 30 mm. The spectral response range of the PMT well matches the wavelength of scintillation light of LYSO at 420 nm.

7.2 Background monitor simulation

After the design components of the background monitors were decided, the detectors were included in the Belle II detector simulation in Geant4. The ECL shields were previously simulated, so the holes which will contain the background monitors were added in the corresponding positions. The 30 mm×30 mm cylindrical LYSO crystals were added in the simulation at the design positions. These crystal elements were simulated as Geant4 sensitive materials, which enables the recording of each interaction of an incoming particle with the crystal. The information about the position of each interaction is recorded, together with the energy deposition in the crystal and the momentum of the incoming particle. Incorporating this into the Belle II simulation enabled the analysis of the interactions of the background particles with the LYSO crystals. Figure 7–2 shows the geometry implementation of the holes and the crystals in the ECL shield simulation.

The background simulation was run with the implemented background monitors. The background types used are Coulomb, Touschek, radiative Bhabha and wide angle Bhabha, which are described in Chapter 4. The total energy deposition per 1 ms for every background type in the LYSO crystals is shown in Fig. 7–3, together with the total number of showers generated by primary background particles. The crystals are labeled from 1 to 8; crystals 1-4 are located in the forward endcap, while the crystals 5-8 are in the backward. The crystals 1, 2, 3, 4 and 5, 6, 7, 8 correspond to the azimuthal positions of 356°, 86°, 176°, 266°, respectively. From the upper graph in Fig. 7–3, the crystals at ϕ=356° receive the highest amount of energy, for

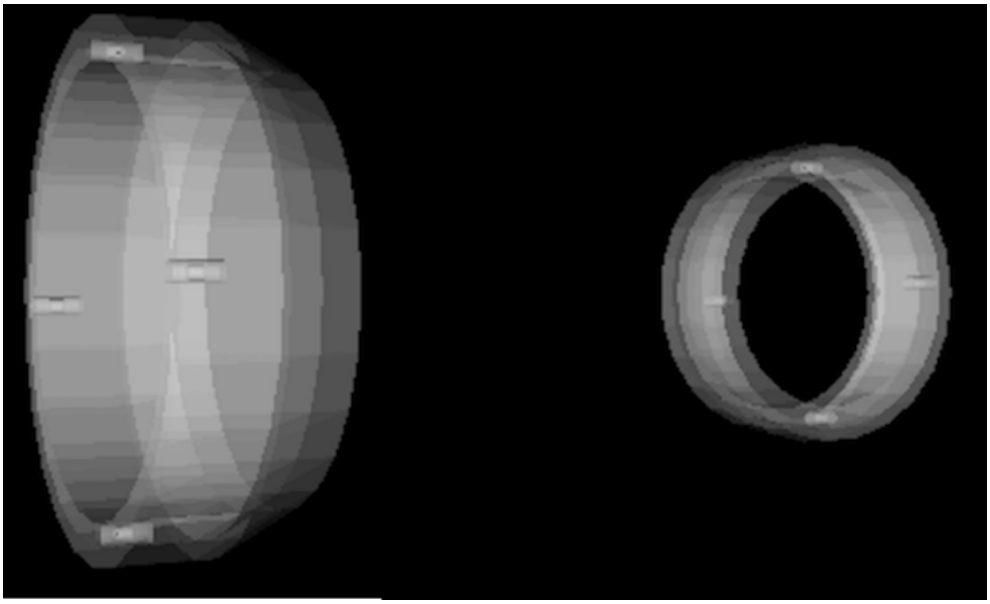

Figure 7–2: The ECL shields simulated in Geant4 with the holes and crystals visible; the inner radius of the forward shield is 73 cm, the thickness of the polyethylene part is 5.1 cm and the thickness of the lead part is 4.3 cm; for the backward shield, the inner radius is 89 cm, the thickness of the polyethylene part is 4.4 cm and the thickness of the lead part is 4.3 cm.

both forward and backward endcap. This agrees with the estimation performed by selecting the ECL crystals that are closest to the background monitors' positions shown in Fig. 6–6. The errors are calculated via the bootstrapping statistical method previously described in Chapter 6. The bottom part in Fig. 7–3 shows the total number of showers generated by primary background particles. The number of hits per crystal is more evenly distributed, meaning that the energy of individual hits in the crystals that receive lower amounts of energy are less energetic on average than the hits in the crystals with higher energy deposition.

Figure 7–4 shows the energy deposition per 1 ms for each crystal separated into

background types. Figure 7–5 shows the z-position of the primary vertex. The Coulomb scattering of the high energy ring produces energy deposits in the backward endcap crystals, with a low energy deposition on the order of 1 MeV per 1 ms. The vertex position is hand-calculated at -122.7 cm. The energy deposition by the showers created by Coulomb scattered low energy ring particles is located primarily in the backward endcap, as in the ECL background simulation shown in Fig. 6–1.

The Touschek background from the high energy ring reaches all the detectors, but deposits less energy than the Touschek background from the low energy ring, in accordance with Equation 4.2. The radiative Bhabha background type deposits the most energy in the background monitors. The background originating from the high energy beam is visible in the forward-endcap crystals, while the low energy beam background is visible in the backward endcap, since the radiative Bhabha interaction occurs at the IP. The wide-angle Bhabha type background is similarly distributed. Compared to the ECL simulation, the wide-angle Bhabha events are not as energetic. This is because the background detectors do not receive direct hits from the bent positron or electron from the beam, but only a remnant of the shower it creates.

The results obtained from the background simulation for the monitors are consistent with the results from the ECL background simulation. They confirm the need for the wide dynamic range of the background monitors, since energy deposits per 1 ms range from 1 MeV to 1 GeV.

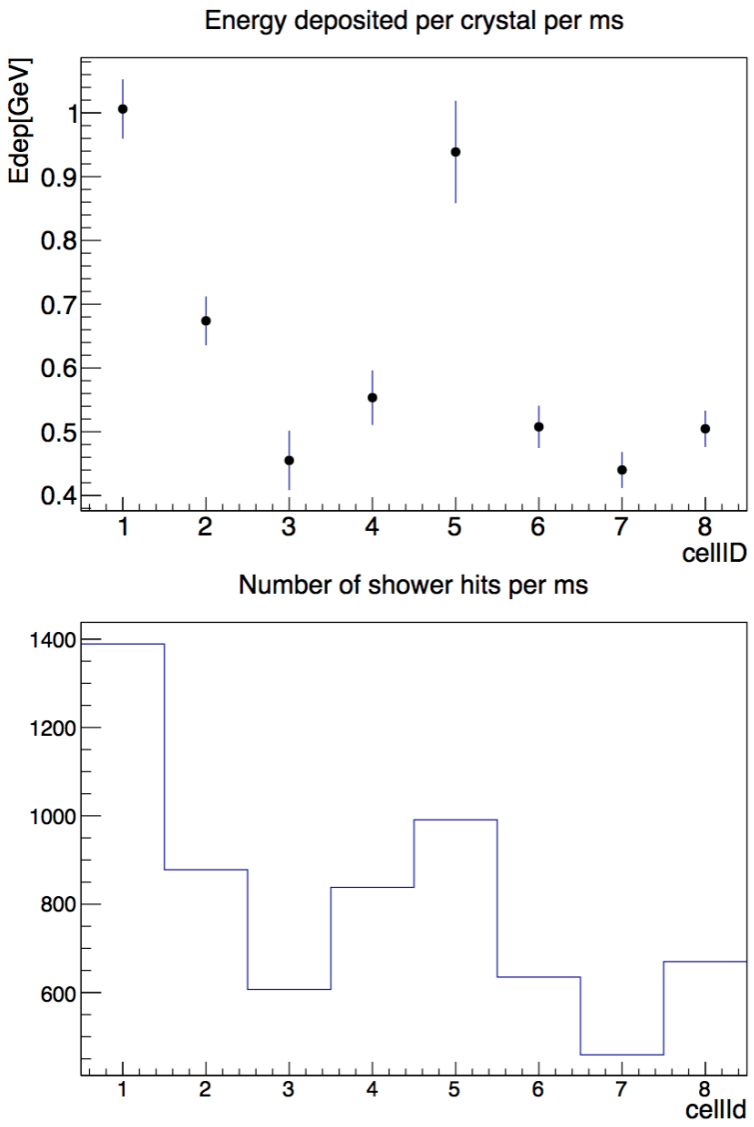

Figure 7–3: The top plot shows the total energy deposited per 1 ms per crystal; x-axis shows the crystal number; y-axis shows the energy in gigaelectronvolts. The bottom plot shows the number of background showers that create interaction in the background monitors' crystals; x-axis shows the crystal number; y-axis shows the number of showers.

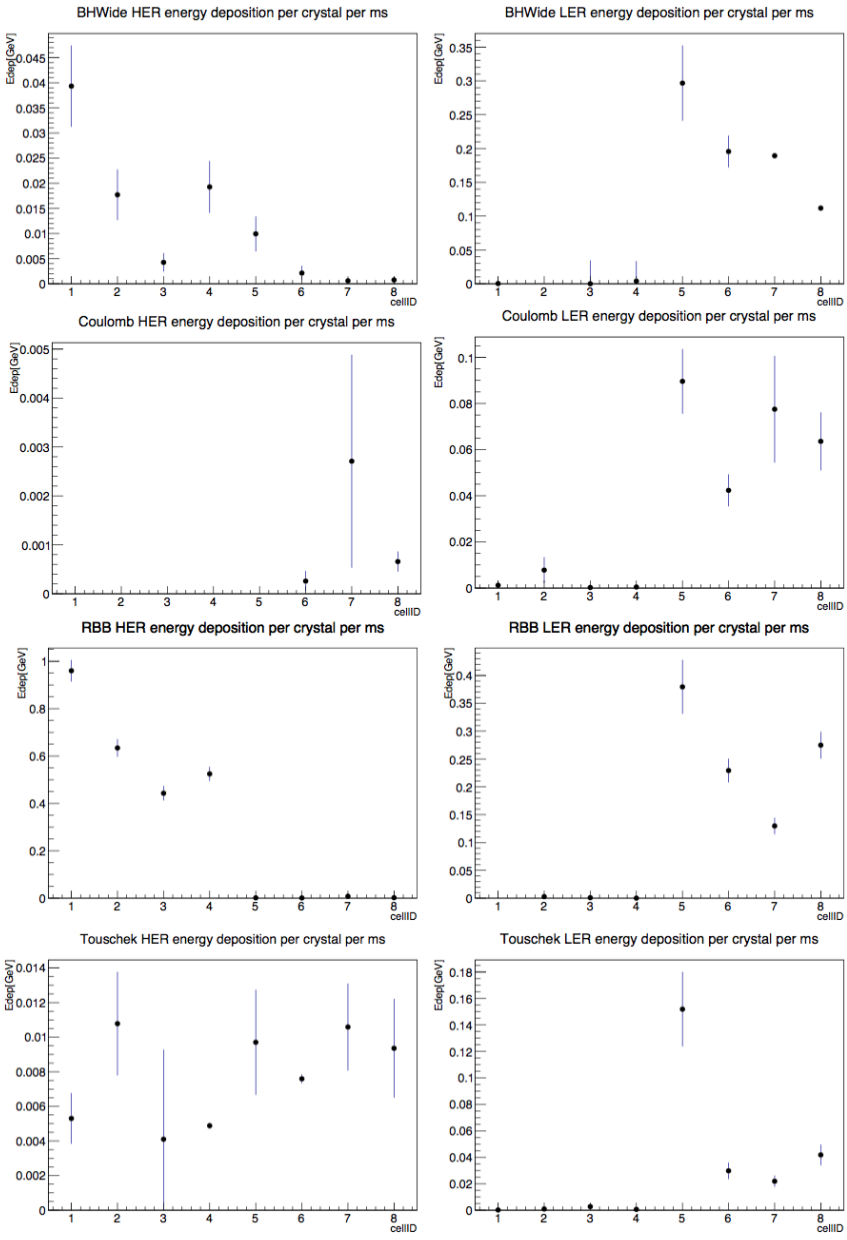

Figure 7–4: Simulated energy deposition per 1 ms for every background type in the eight crystals of the background monitors; x-axis shows the crystal number; y-axis shows the energy in gigaelectronvolts. The plots on the left show the energy deposition originating from the high-energy beam interactions, while the plots on the right show the energy deposition originating for the low-energy beam interactions. Errors are calculated by using the bootstrap statistical method.

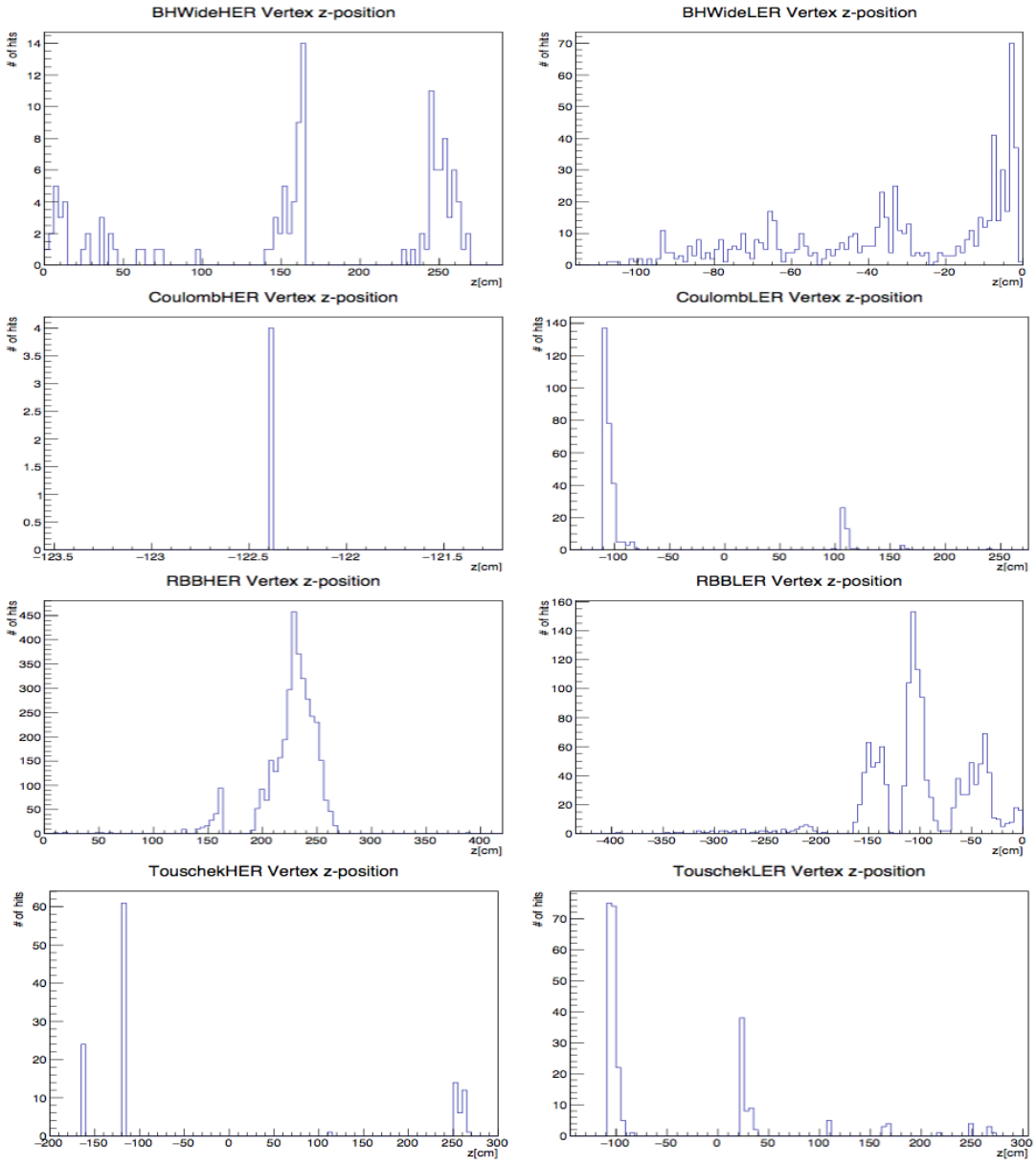

Figure 7–5: Simulated position of the primary vertex on the z-axis for every background type that creates showers that deposit energy in the background monitors. The x-axis shows the z-position of the primary vertex, while the y-axis shows the number of primary vertices at the given position. The plots on the left show the vertices for the high-energy beam, while the plots on the right show the vertices for the low-energy beam.

CHAPTER 8
Conclusion

The primary objective of the thesis was to describe the design and simulation process of the beam-background monitors in the vicinity of the electromagnetic calorimeter of the Belle II experiment. The initial design of the monitors was explained, together with their implementation in the existing Belle II detector simulation.

The main sources of beam background are expected to be the Coulomb, Touschek and Bhabha scatterings, together with the background coming from the beam injection. The beam-background monitors are needed in the area near the calorimeter endcaps in order to provide information about the radiation environment inside the detector to the SuperKEKB operators. The monitors are to be placed in recesses in the polyethylene part of the endcap shields. The analysis of the ECL background simulation showed there is no preferential azimuthal placement of the detectors. The even distribution of the detectors around the azimuthal angle ϕ was chosen, with the final positions being at $\phi = \{356^\circ, 86^\circ, 176^\circ, 266^\circ\}$ at each endcap, giving eight detectors in total. The ECL simulation also confirmed the need for wide dynamic range of the detectors, with the energy deposition by different background types varying from 1 MeV to 1 GeV per millisecond. LYSO crystal was chosen as the scintillating material, which will be read out by the Hamamatsu R7761-70 photomultiplier tube. Together with its radiation hardness and high light yield, LYSO crystal has ideal

decay timing of 40 ns, which well matches the need of timing resolution below 100 ns in order to distinguish between the injection background from the two topped-up bunches. The R7761-70 PMT is suitable for use in the high magnetic field present in the Belle II detector. It has high gain and spectral range that matches the wavelength of emitted scintillation light from LYSO crystals. The background monitors were implemented in the simulation of the Belle II detector. The background simulation of the monitors confirmed the findings from the ECL background simulation. The next steps in this project are the lab testings of the proposed design. The LYSO and photomultiplier setup will be tested in a high magnetic field environment using a radiation source to simulate the background radiation. A calibration method for the detectors will be developed. The testing, calibration and design of readout electronics will be done in collaboration with the Belle II group at the Université de Montréal. The installation on site will be performed during the Summer of 2017, before the start of the Phase II commissioning operation in late Fall 2017. Budgetary restrictions permit only four detectors to be installed at this time, with the possibility of adding the remaining four before the start of the full Belle II experiment in late 2018.

APPENDIX A
Technical drawing of the Belle II detector

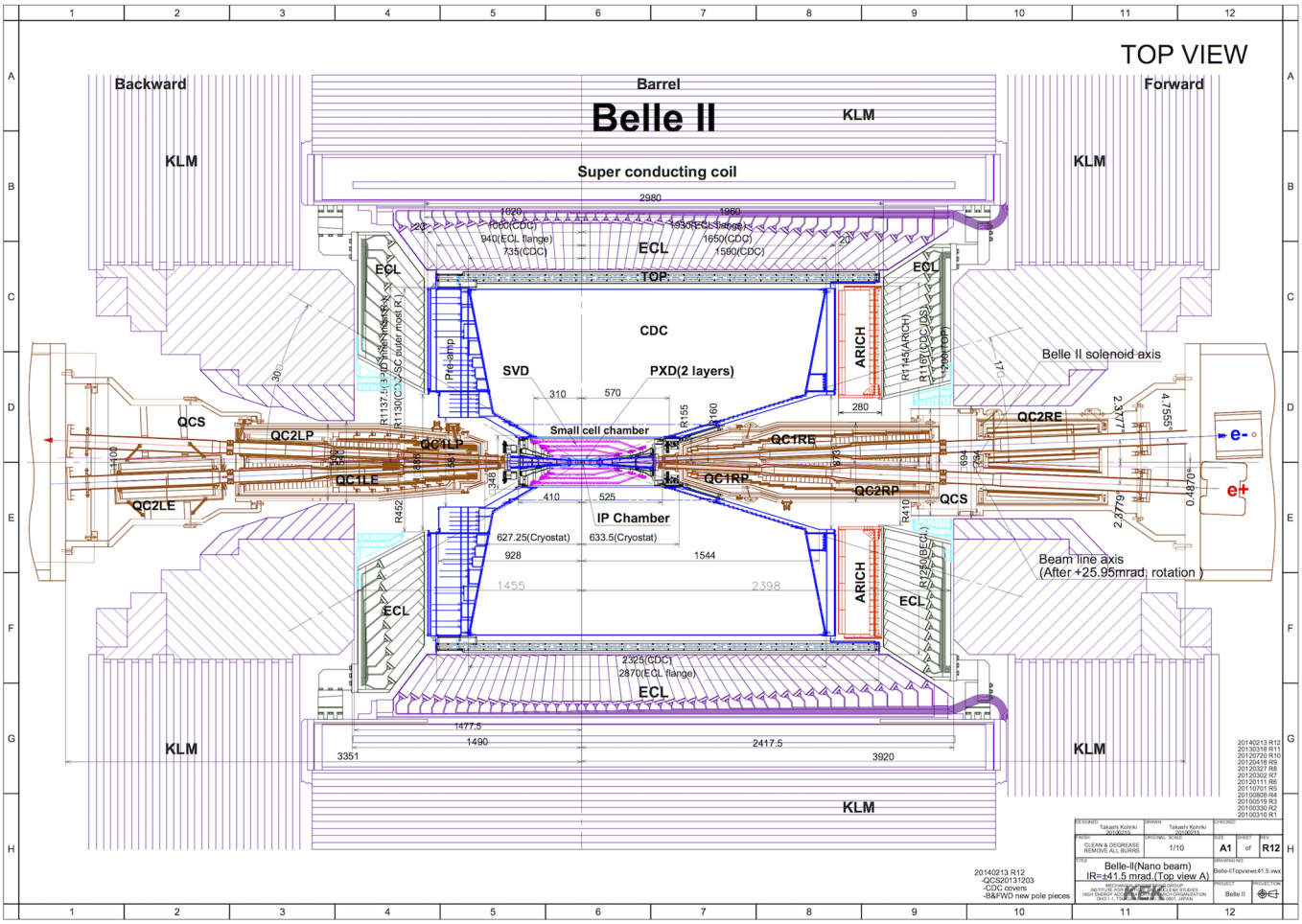

Figure A–1: Technical drawing of the Belle II detector; the ECL shields are drawn in light blue. [1]

Acronyms

ARICH Aerogel Ring-Imaging Cherenkov Detector.

BEAST II Beam Exorcism for A STable experiment II.

CDC Central Drift Chamber.

CP Charge-Parity symmetry.

DEPFET Depleted Field Effect Transistor.

ECL Electromagnetic Calorimeter.

HDPE high-density polyethylene.

HER High Energy Ring.

IP Interaction Point.

IR Interaction Region.

KLM K_L^0 and μ detector.

LER Low Energy Ring.

LYSO lutetium-yttrium oxyorthosilicate.

PID Particle Identification.

PMT photomultiplier tube.

PXD Pixel Vertex Detector.

QCS final focus quadrupole magnets.

RBB Radiative Bhabha.

RPC Resistive Plate Chambers.

SR Synchrotron Radiation.

SVD Silicon Vertex Detector.

TMCI Transverse Mode Coupling Instability.

TOP Time of Propagation.

VXD Vertex Detector.

References

[1] T. Abe, I. Adachiand K. Adamczyk, H. Aihara S. Ahn, K. Akai, M. Aloi, L. Andricek, K. Aoki, Y. Arai, et al. Belle II technical design report. *ArXiv:1011.0352*, 2010.

[2] Y. Ohnishi, T. Abe, T. Adachi, K. Akai, Y. Arimoto, K. Ebihara, K. Egawa, J. Flanagan, H. Fukuma, Y. Funakoshi, et al. Accelerator design at SuperKEKB. *Progress of Theoretical and Experimental Physics*, 2013(3):3–11, 2013.

[3] S. Hashimoto, M. Hazumi, J. Haba, J.W. Flanagan, and Y. Ohnishi. Letter of intent for KEK Super B Factory. Technical report, High Energy Accelerator Research Organization, 2004.

[4] J. Beringer, J-F Arguin, R.M. Barnett, K. Copic, O. Dahl, D.E. Groom, C-J Lin, J. Lys, H. Murayama, C.G. Wohl, et al. Review of particle physics particle data group. *Physical Review D (Particles, Fields, Gravitation and Cosmology)*, 86(1), 2012.

[5] T. Ieiri, T. Kawamoto, and K. Hirata. Measurement of the beam-beam parameter by exciting coherent betatron oscillation. *Nuclear Instruments and Methods in Physics Research Section A: Accelerators, Spectrometers, Detectors and Associated Equipment*, 265(3):364–370, 1988.

[6] D. M. Asner, R. A. Briere, J. E. Fast, et al. US Belle II project technical design report, 2013. `http://belleweb.pnnl.gov/forTDRreview/TDR-SLAC-13Dec8.pdf`,Accessed: 2016-11-10.

[7] Belle II Collaboration. BEAST webhome. `https://confluence.desy.de/display/BI/BEAST+WebHome`,Accessed: 2016-10-20.

[8] A. Abashian, K. Gotow, N. Morgan, L. Pillonen, S. Schrenk, K. Abe, I. Adachi, J.P. Alexander, K. Aoki, S. Behari, et al. The Belle detector. *Nuclear Instruments and Methods in Physics Research Section A: Accelerators, Spectrometers, Detectors and Associated Equipment*, 479(1):117–232, 2002.

[9] B. Aubert, A. Bazan, A. Boucham, D. Boutigny, I. De Bonis, J. Favier, J-M. Gaillard, A. Jeremie, Y. Karyotakis, T. Le Flour, et al. The BABAR detector. *Nuclear Instruments and Methods in Physics Research Section A: Accelerators, Spectrometers, Detectors and Associated Equipment*, 479(1):1–116, 2002.

[10] K. Abe, R. Abe, I. Adachi, B.S. Ahn, H. Aihara, M. Akatsu, G. Alimonti, K. Asai, M. Asai, Y. Asano, et al. Observation of large CP violation in the neutral B meson system. *Physical Review Letters*, 87(9):91–802, 2001.

[11] B. Aubert, R.K. Yamamoto, N. Danielson, G. Cavoto, D. Monorchio, V. Eschenburg, S. T'Jampens, N.S. Knecht, M. Haire, M.V. Purohit, et al. Observation of direct CP violation in $B^0 \to K^+\pi^-$ decays. Technical report, 2004.

[12] Belle II Collaboration. Belle II 3D model. `https://www.belle2.org/e21595/e21770/infoboxContent25428/BelleII3D.pdf`, Accessed: 2016-12-01.

[13] C. Mariñas and M. Vos. The Belle II DEPFET pixel detector: A step forward in vertexing in the superkekb flavour factory. *Nuclear Instruments and Methods in Physics Research Section A: Accelerators, Spectrometers, Detectors and Associated Equipment*, 650(1):59–63, 2011.

[14] M. Friedl, K. Ackermann, H. Aihara, T. Aziz, T. Bergauer, A. Bozek, A. Campbell, J. Dingfelder, Z. Drasal, A. Frankenberger, et al. The Belle II silicon vertex detector. *Nuclear Instruments and Methods in Physics Research Section A: Accelerators, Spectrometers, Detectors and Associated Equipment*, 732:83–86, 2013.

[15] K. Inami et al. TOP counter for particle identification at the Belle II experiment. *Nuclear Instruments and Methods in Physics Research Section A: Accelerators, Spectrometers, Detectors and Associated Equipment*, 766:5–8, 2014.

[16] S. Nishida, I. Adachi, N. Hamada, T. Iijima K. Hara, S. Iwata, H. Kakuno, H. Kawai, S. Korpar, P. Kriz, et al. Aerogel RICH for the Belle II forward PID. *Nuclear Instruments and Methods in Physics Research Section A: Accelerators, Spectrometers, Detectors and Associated Equipment*, 766:28–31, 2014.

[17] S.K. Sahu. A generator for study of background due to beam-gas interaction at KEK B-factory. *Belle note 97-172*, 1997.

[18] H. Wiedemann. *Particle accelerator physics*. Springer, 2015.

[19] H. Nakayama, Y. Suetsugu, K. Kanazawa, Y. Ohnishi, Y. Funakoshi, K. Ohmi, D. Zou, et al. Small-beta collimation at SuperKEKB to stop beam-gas scattered particles and to avoid transverse mode coupling instability. In *Proceedings of IPAC2012*, 2012.

[20] F. Ruggiero. Transverse mode coupling instability due to localized structures. *Particle Accelerators*, 20(CERN-LEP-TH-84-21):45–64, 1984.

[21] A. Piwinski. The Touschek effect in strong focusing storage rings. *ArXiv:9903034*, 1999.

[22] H. Nakano, H. Yamamoto, K. Kanazawa, H. Nakayama, Y. Ohnishi, C. Kiesling, S. Koblitz, A. Moll, and M. Ritter. Beam background simulation for SuperKEKB/Belle-II. *Proceedings of IPAC2011*, 3, 2011.

[23] G.R. Blumenthal and R.J. Gould. Bremsstrahlung, synchrotron radiation, and Compton scattering of high-energy electrons traversing dilute gases. *Reviews of Modern Physics*, 42(2):237, 1970.

[24] H. Nakayama, Y. Funakoshi, Y. Onishi, K. Kanazawa, and T. Ishibashi. SuperKEKB background simulation, including issues for detector shielding. *Proceedings of HF2014*, 3, 2014.

[25] S. Actis, P. Mastrolia, and G. Ossola. NLO QED Corrections to Hard-Bremsstrahlung Emission in Bhabha Scattering. *Physics Letters B*, B682:419–427, 2010.

[26] C. Grupen and I. Buvat. *Handbook of particle detection and imaging*. Springer Science & Business Media, 2011.

[27] K.Hirata et al. An introduction to SAD. In *2nd Advanced ICFA Beam Dynamics Workshop on Aperture-Related Limitations of the Performance and Beam Lifetime in Storage Rings*, pages 62–65, 1988.

[28] R. Kleiss and H. Burkhardt. BBBREM-Monte Carlo simulation of radiative Bhabha scattering in the very forward direction. *ArXiv:9401333*, 1994.

[29] S. Jadach, W. Płaczek, and B.F.L. Ward. Bhwide 1.00: O (α) YFS exponentiated Monte Carlo for Bhabha scattering at wide angles for LEP1/SLC and LEP2. *Physics Letters B*, 390(1):298–308, 1997.

[30] S. Agostinelli, J. Allison, K. Amako, J. Apostolakis, H. Araujo, P. Arce, M. Asai, D. Axen, S. Banerjee, G. Barrand, et al. GEANT4a simulation toolkit. *Nuclear instruments and methods in physics research section A: Accelerators, Spectrometers, Detectors and Associated Equipment*, 506(3):250–303, 2003.

[31] R. Brun and F. Rademakers. ROOT - an object oriented data analysis framework. *Nuclear Instruments and Methods in Physics Research Section A: Accelerators, Spectrometers, Detectors and Associated Equipment*, 389(1):81–86, 1997.

[32] R. Ping. Event generators at BESIII. *Chinese Physics C*, 32(08):599–602, 2008.

[33] D.R. Yennie, S. Frautschi, and H. Suura. The infrared divergence phenomena and high-energy processes. *Annals of Physics*, 13(3):379–452, 1961.

[34] B. Efron and R. Tibshirani. Bootstrap methods for standard errors, confidence intervals, and other measures of statistical accuracy. *Statistical Science*, pages 54–75, 1986.

[35] J. Chen, R. Mao, L. Zhang, and R-Y. Zhu. Large size LSO and LYSO crystals for future high energy physics experiments. *IEEE Transactions on Nuclear Science*, 54(3):718–724, 2007.

[36] K. Kossert, G. Jörg, and C. Gostomski. Experimental half-life determination of ^{176}Lu. *Applied Radiation and Isotopes*, 81:140–145, 2013.

[37] Q. Wei. Intrinsic radiation in lutetium based PET detector: Advantages and disadvantages. *ArXiv:1501.05372*, 2015.

[38] Hamamatsu Photonics K.K. Hamamatsu Photomultiplier tubes catalog. `http://www.hamamatsu.com/resources/pdf/etd/PMT_TPMZ0002E.pdf`, Accessed: 2016-12-01.